Feasibility Study of the $(\alpha, \alpha'\gamma)$ reaction at $\theta_{lab} = 0^\circ$ Using the K600 Magnetic Spectrometer

by

Wade Luke Erasmus

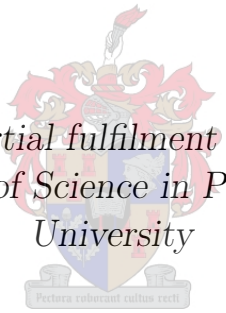

Thesis presented in partial fulfilment of the requirements for the degree of Master of Science in Physics at Stellenbosch University

Department of Physics,
University of Stellenbosch,
Private Bag X1, Matieland 7602, South Africa.

Supervisor: Prof. Paul Papka, *Dept. Physics*

March 2015

Declaration

By submitting this thesis electronically, I declare that the entirety of the work contained therein is my own, original work, that I am the owner of the copyright thereof (unless to the extent explicitly otherwise stated) and that I have not previously in its entirety or in part submitted it for obtaining any qualification.

Date: .....

Abstract

Feasibility Study of the (α, $\alpha'\gamma$) reaction at $\theta_{lab} = 0°$ Using the K600 Magnetic Spectrometer

W. L. Erasmus

Department of Physics,
University of Stellenbosch,
Private Bag X1, Matieland 7602, South Africa.

Thesis: MSc

March 2015

The coincident measurement of gamma-rays originating from nuclei excited in light-ion reactions and scattered alpha-particles presents interesting opportunities to characterize the decay path for low multi-polarity nuclear excitations. This coincident measurement at $\theta_{lab} = 0°$ was shown to be a powerful tool for the spectroscopy of isoscalar E1 transitions, being selective to distinct modes of bulk nuclear motions. Aided with the high resolution capabilities provided by the HPGe Clover detectors as well as the K600 magnetic spectrometer for both γ and charged particle detection, these experiments are motivated by the need to investigate E1 strength in stable nuclei around the particle emission threshold, more commonly referred to as the Pygmy Dipole Resonance (PDR). However, due to our detector configuration we find that higher efficiency detectors offer a better overall functionality in these $\alpha - \gamma$ coincidence measurements which specifically suffer from low statistics.

The feasibility of the (α, $\alpha'\gamma$) reaction using high resolution Clover detectors and the high efficiency HAGAR detector is characterized through their efficiency to detect γ rays in coincidence with the K600 magnetic spectrometer at $\theta_{lab} = 0°$. Through the construction of $E_\gamma - E_X$ coincidence matrices,

decay transitions of closely lying nuclear excitations can be studied on a state-by-state basis. The result is a quantified representation of γ yield, of which optimization is the key focus in order to extract meaningful nuclear structure information.

Opsomming

n' Uitvoerbaarheidstudie vir die ondersoek van die $(\alpha, \alpha'\gamma)$ reaksie by $\theta_{lab} = 0^\circ$ met behulp van die K600 Magnetiese Spectrometer

W. L. Erasmus

Fisika Departement,
Universiteit van Stellenbosch,
Privaatsak X1, Matieland 7602, Suid Afrika.

Tesis: MSc

Maart 2015

Die samevallende meting van gammastrale van kerne opgewek in die lig-ion reaksies en verspreide alfa-deeljties, bied interessante geleenthede aan om die verval pad vir lae multi-polariteit kern opwekkings te karakteriseer. Hierdie samevallende meting by $\theta_{lab} = 0^\circ$ was getoon om 'n kragtige instrument vir die spektroskopie van isoscalar E1 oorgange te wees, as gevolg van die vermoë om selektief te onderskei tussen modes van kollektiewe kern ossillasies. Aangehelp met die hoë resolusie moontlikhede wat deur die HPGe Clover detektors asook die K600 magnetiese spektrometer vir beide γ en gelaaide deeltjie opsporing, hierdie eksperimente is gemotiveer deur die behoefte om E1 krag te ondersoek in stabiele kerne rondom die deeltjie emissie drumpel, meer algemeen na verwys as die Pygmy Dipool Resonansie (PDR). Maar as gevolg van die detektor opset, vind ons dat 'n hoër doeltreffendheid detector 'n beter algehele funksionaliteit aanbied wat in hierdie samevallende metings veral belangrik is weens lae statistiek.

Die haalbaarheid van die reaksie wat gebruik maak van hoë resolusie Clover detektors en die hoë doeltreffendheid HAGAR detektor word gekenmerk

deur hul doeltreffendheid om gammastrale optespoor in toeval met die K600 magnetiese spektrometer by $\theta_{lab} = 0°$. Deur die konstruksie van toeval $E_\gamma - E_X$ matrikse, verval oorgange van kern opwekkings kan op 'n staat-by-staat basis bestudeer word. Die resultaat is 'n gekwantifiseerde verteenwoordiging van γ opbrengs, waarvan optimalisering die sleutel fokus is om betekenisvolle kernstruktuur inligting te kan onttrek.

Acknowledgements

I'm grateful to the following:

My supervisor Prof. Paul Papka and iThemba LABS for allowing me the opportunity to work on such an interesting project.

The National Research Foundation (NRF) and Department of Science and Technology (DST) for financial support during my MSc.

Dr. Retief Neveling from iThemba LABS for his willingness to advice and assist me with the data analysis and any K600 related queries.

Dr Phil Adsley for his constant aid and speedy responses.

My family for their patience and support throughout my entire study career.

The one person who always believed in me, who sacrificed a lot to make this possible and who never hesitated to assist in any way, thank you so much Carryn Edith Adams.

My office mates and friends for the encouragement, motivation and interesting talks.

Christine Ruperti for her enthusiastic support willingness to always lend a helping hand. You are the engine of this department!

Finally, Prof. Paul Papka, for his guidance, support and patience during the entire course of my MSc work. Your insight and expertise are invaluable and I deeply appreciate everything.

Dedications

This thesis is dedicated to my late grandfather,
Ronald Alfred Fraser.

O Lord my God, when I in awesome wonder, consider all the worlds Thy Hands have made. I see the stars, I hear the rolling thunder, Thy power throughout the universe displayed. Then sings my soul, my Saviour God, to Thee! How great Thou art, how great Thou art...

Contents

List of Figures

List of Tables

Chapter 1

Introduction

Through the subject of nuclear reactions, the fundamentals of nuclear structure are revealed. Over the decades the complexity of nuclei and the vast knowledge it conceals, reshaped the way we think about matter and our universe. From the early naive picture of the atom to the first pioneering nuclear scattering experiments performed by Rutherford, the structure of the nucleus was revealed through inspection of probes directed at target nuclei. The scattering of nuclei in nuclear reactions paints us a brief microscopic picture of the nucleus and provides us with great insight into the invisible forces at work here.

Nuclear reactions proceed through many possible distinct mechanisms but can be subdivided quantitatively into two main classes, namely, direct reactions and compound nuclear reactions. The case of complete kinetic energy transfer between the projectiles and target nuclei where the initial and final particles are identical, are referred to as elastic scattering reactions. Similarly, inelastic scattering reactions refer to interactions where the partial kinetic energy transferred by the projectile is used in the excitation of the target nuclei. Thus the final products of the reaction are the same as the initial, except one or more particles are left in an excited state. Consequently, the excited target nucleus returns to its ground state through emission of one or more γ rays. Elastic and inelastic scattering are types of direct reactions [1].

This investigation is concerned with the inelastic scattering of nuclei coupled with the coincident detection of γ rays emitted from excited target nuclei states, specifically the ^{24}Mg(α, $\alpha'\gamma$) inelastic scattering reaction. The experiment was performed at a spectrometer angle of 0° with a 160 MeV α-particle beam. Similar reactions were successfully performed, however, during this time the study of early resonance structures did not necessitate higher energy resolution [2, 3]. With the advent of improved (α, $\alpha'\gamma$) experimental techniques, the combination of γ spectroscopy with inelastic α-particle scattering at $\theta_{lab} = 0°$

proved to be a powerful tool for the spectroscopy of isoscalar E1 transitions [4, 5]. Furthermore, these E1 transitions are closely linked to E1 strength in both stable and unstable nuclei around the particle emission threshold, now referred to as the Pygmy Dipole Resonance (PDR) (see e.g. [6–8]). The remainder of this chapter will be dedicated to outlining the theory applicable to this investigation. This framework includes a detailed description of inelastic scattering as a direct nuclear reaction in section 1.1. In section 1.2 a brief introduction to Coulomb interactions is necessary for the description of nuclear excitations. The $(\alpha, \alpha'\gamma)$ reaction which is further delved into in section 1.3, is used to characterize certain observables of the reaction with emphasis on forward scattering angles. Specifically, we introduce the concept of angular distribution in the coincident measurement of γ rays from excited states, to characterize the multi-polarity of the transitions from the individual excitations. Furthermore, this study allows us to access and view certain features of the PDR, of which will be discussed too.

1.1 Inelastic Scattering as a Direct Reaction

As mentioned elastic and inelastic scattering are types of direct reactions where the final and initial particles are the same chemical species. However, for inelastic scattering one or more of the final particles may be in an excited state. The particle is thus scattered into a different exit channel from the incident one and the reaction proceeds as follows

$$a + A \Rightarrow a +^{*} A \quad , \tag{1.1.1}$$

where a is the projectile and A the target nucleus, with $^{*}A$ denoting the target nucleus in an excited state. Direct reactions are distinguished by the duration of the interaction and are considered to be relatively prompt (10^{-22} s), which is characteristic of the time taken for a projectile of a few MeV to transit the diameter of the target nucleus [9].

The theoretical interpretation of direct reactions is rooted in the assumption that the projectile experiences the average potential of the target nucleus [1]. This interaction is describable via an interaction potential within the framework of the optical model. Such a potential inherently makes provision for a range of non-elastic processes including inelastic scattering. Thus without penetrating the interior of the target nucleus, the projectile interacts with the target at its surface, generally making inelastic scattering more surface localized (i.e. peripheral interactions) [10]. As opposed to compound nuclear reactions possessing an isotropic angular distribution, the yield of particles

in direct reactions are predominantly in a forward direction relative to the projectile. This translates to the differential cross sections of direct reactions being peaked in the forward direction, falling rapidly away with increasing angle (refer to Fig. 1.1 [9]).

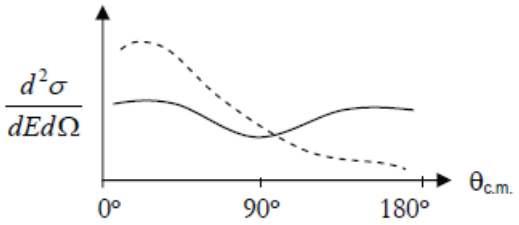

Figure 1.1: *Typical direct (dashed line) and compound (solid line) reaction cross sections of as a function of the centre of mass angle.*

1.2 Selective Modes of Excitation

There exists a certain critical distance of approach for the incidental α particles, at which scattering falls below the coulomb value. It is assumed that this distance is closely related to the nuclear radius and that for this scenario strong absorption sets in [13]. For an optimum window but not within this critical distance, high energy α particles are affected by the strong nuclear interaction even in glancing collisions. Consequently, this restricts interference effects between the incident α particles and the target nucleus to the rim of the nucleus [10]. For this critical distance, $r \approx R$, where r is the distance of approach, at high incident energies inelastic scattering is the dominant process of interaction. Coupled with the fact that this investigation takes place at a spectrometer angle of zero degrees (i.e. $\theta_{lab} = 0°$) enhances the experimental methods selectivity towards low-lying nuclear excitations. Inherently, the isoscalar dipole strength is at a maximum at very forward angles [4], since it is here that the $L = 0$ (L referring to the total angular momentum) angular distribution peaks and that states of a natural parity character are enhanced. Thus the electric-dipole (E1) strength transitions are a prominent feature of the experimental technique and are predominantly evident in the excitation process.

Inelastic scattering preferentially excites collective modes within the nucleus, of which electric-dipole (E1) moments are a distinct feature [11]. Collective phenomena are rooted in the idea that apart from the motion of individual nucleons outside closed shells, the nuclear core too portrays a collective motion and it is the interaction between these two types of motions that results in the

permanent deformation of the nucleus. The motion of individual nucleons is regarded and is describable as a shell model feature, while the collective behavior of the nuclear core is closely related to the strong interaction model. Subsequently, this idea of nuclear deformation via a collective motion is a combination of the two competing models [10]. Fig 1.2 [10] illustrates how a nucleus deforms in relation to its potential energy.

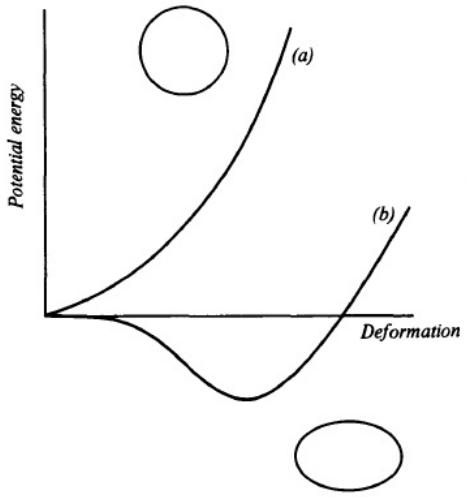

Figure 1.2: *Illustration of the deformation of the nucleus in relation to its potential energy. For a deformation of the core, the outer nucleons move to orbits of larger radius thus the kinetic energy decreases as the radius increases.*

1.2.1 Examples of Collective Excitation Modes

Giant resonances (GR's) as a collective excitation mode are shape oscillations around the equilibrium of nuclear systems and are prominent features of nuclear spectra at excitation energies exceeding the nucleon binding energy. They provide information on the bulk properties of a particular nucleus and are often seen as states of several MeV width characteristic of excitations extending over one or two major shells.

The well known giant resonance is the so-called Isovector Giant Dipole Resonance (IVGDR). It is regarded as a collective dipole oscillation of protons versus neutrons well above the particle threshold resulting in a dynamic electric-dipole (E1) moment. The phenomenon has been extensively studied over the years providing evidence that it is indeed a global feature of all nuclei [4, 11].

In the energy region between the GDR and the particle decay threshold there exists a low-lying concentration of dipole strength, now known to be a manifestation of a recently discovered nuclear excitation mode. Aided by recent

advances in Nuclear Resonance Fluorescence (NRF) techniques as well as Coulomb dissociation the collective mode is referred to as the Pygmy Dipole Resonance (PDR) [12]. Based on several theoretical analysis the PDR is predicted as the resonant oscillation of the weakly-bound neutron skin against a symmetric proton-neutron core with $T = 0$ isospin character. In this instance for the understanding of the collective model it is vital to envision a clear separation between the individual motion of the outer neutron skin and the inner collective core [8].

1.3 The $(\alpha, \alpha'\gamma)$ Reaction

Pioneering experiments performed by Poelhekken et al. [4] has proven the combination of γ spectroscopy with inelastic α-particle scattering to be a powerful tool for the investigation of bound isoscalar E1 transitions. This is possible due to the excellent selectivity of the $(\alpha, \alpha'\gamma)$ reaction to low-spin states. One important piece of information required to settle the nature of the low-lying strength is the identification of the isospin structure. The $\alpha - \gamma$ angular correlation of the decay to a 0^+ ground state allows the unique assignment of the multi-polarity of the excited state.

Decay schemes involving electromagnetic radiation is an ideal source of information, since spin and parity changes not only allows us to determine multi-polarity but also the electric and magnetic character of the radiation [13]. From a view point of the semi-classical theory of radiation, for radiation of multi-polarity $(\boldsymbol{L}, \boldsymbol{M})$ for a transition between nuclear states with spin $(I_i m_i)$ and $(I_f m_f)$ there exists a well defined angular distribution $F_L^M(\theta)$. In turn these transitions are based on the conservation of angular momentum and parity given by the selection rules relating the quantum numbers in the following manner

$$I_i + I_f \geq \boldsymbol{L} \geq |I_i - I_f| \tag{1.3.1}$$

$$m_f - m_i = \boldsymbol{M} \quad , \tag{1.3.2}$$

where $|\boldsymbol{M}| \geq \boldsymbol{L}$. Here $\boldsymbol{M}$ refers to the multi-polarity and $\boldsymbol{L}$ to the total angular momentum. It is evident from the above expressions that the multi-polarity $\boldsymbol{M}$ is limited in the number of allowed transitions (See Fig. 1.3).

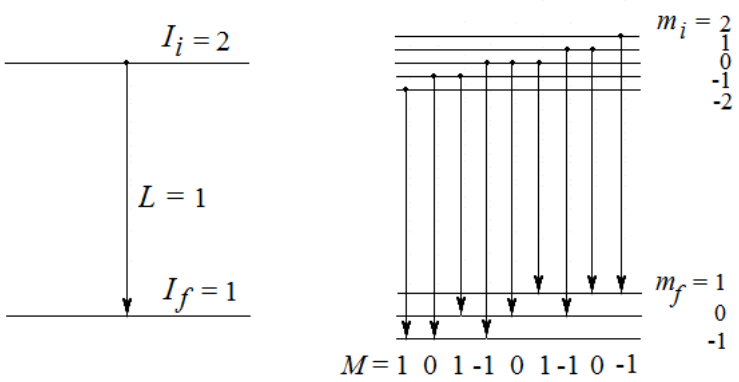

Figure 1.3: *Allowed transitions with specific spin, angular momentum and multi-polarity assignment.*

1.4 Aims of this Study

Outlined in the above sections, it can be seen that the $(\alpha, \alpha'\gamma)$ reaction at a spectrometer angle of 0° provides us with a sound experimental platform from which to perform the spectroscopy of low-lying E1 strength transitions. It was shown that measurements performed at very forward angles enhances the selectivity for low multi-polarity nuclear excitations [5]. Thus with the specific method described in the previous sub-sections, through the coincident measurement of inelastically scattered α particles with γ decays to 0^+ ground states, the characteristic $\alpha - \gamma$ angular correlation allows us to uniquely identify the decay path of low multi-polarity nuclear de-excitations. Furthermore, this selectiveness property aided by the high resolution capabilities of the experimental technique, allows us to carry out a detailed state-by-state analysis of each single transition from which cross sectional data can be attained.

The need to investigate E1 strength in stable nuclei around the particle emission threshold was limited to nuclei with low level density but with improved resolution techniques, this region in the excitation spectra (referred to as the Pigmy Dipole Resonance) can now be investigated for nuclei in the higher mass region. Pioneering experiments at KVI yielded interesting information on the nature of the PDR in N = 82 isotones [11] and ^{124}Sn [12]. The data clearly suggests that the PDR splits up into two well separated groups. It is considered that the low-lying group of states represents the isoscalar neutron skin oscillations while the higher lying group belongs to the tail of the isovector Giant Dipole Resonance (GDR).

Due to the low excitation energies attainable through this experimental technique, these features of the PDR are accessible to this investigation. Furthermore, results obtained here could be compared to nuclear resonance fluorescence (NRF) experimental results, through which the behavior of the PDR is already well known.

The aim of this project is to present a feasibility study as to whether an investigation of the $(\alpha, \alpha'\gamma)$ reaction, with the aid of the K600 magnetic spectrometer, high resolution HPGe Clover detectors and the high efficiency HAGAR detector, can reproduce results of a comparable nature and quality to similar experiments with the same outcomes. The knowledge obtained in this study would further aid future investigations of a similar nature and variations there of. Ultimately it would be interesting to investigate this phenomenon utilizing the $(p, p'\ \gamma)$ reaction.

The experimental setup of the ^{24}Mg$(\alpha, \alpha'\gamma)$ reaction is outlined in chapter 2. This chapter also deals with the data acquisition and experimental procedure involved here with. In chapter 3 the details of analyzing the measured data is described. The results obtained in this investigation and the subsequent theoretical framework modeling the reaction are presented in chapter 4, while chapter 5 contains the conclusion of the feasibility study and prospects of future work.

Chapter 2

Experimental Details

Inelastic *(p, p′)* scattering techniques and corresponding experimental setups at $\theta_{lab} = 0°$ has recently been achieved with the K600 Magnetic Spectrometer at iThemba LABS (Laboratory for Accelerator Based Sciences) [14]. This being realized, together with recent successful development runs for high energy-resolution inelastic α scattering at finite angles, paves the way for inelastic α scattering at $\theta_{lab} = 0°$.

With this proposed experimental technique of high energy-resolution inelastic α scattering at $\theta_{lab} = 0°$, comes the prospect to investigate the coincident measurement of photon decay for nuclei excited in the *(α, α′)* reaction and the detection capabilities that comes herewith.

The experiment which was conducted at iThemba LABS, situated in the Western Cape, South Africa, therefore consists of placing two HPGe Clover detectors and a large NaI crystal from HAGAR at strategic backward angles around the reaction chamber to detect γ rays in coincidence with the K600 Magnetic Spectrometer. The spectrometer, positioned at $\theta_{lab} = 0°$, is instrumented with a focal plane detector array for charged particle detection and operated in the high dispersion focal plane. Reaction products are further identified using time-of-flight techniques.

Data acquisition was conducted over the weekends of 7-9 and 14-16 December 2012 and involved the merging of the digital XIA data acquisition system (DAQ) with the Versa Modula Europa (VME) based DAQ of the K600. Consequently, the XIA DAQ will be for the data acquisition of the auxiliary γ-ray detectors. The full electronic setup and the method of data acquisition as well as the details involving all these experimental elements are further discussed in the remainder of this chapter.

2.1 Particle Beam and Targets

At iThemba LABS, the main accelerator facility hosts two Solid Pole Injector Cyclotrons (SPC1 and SPC2) and a single Separated Sector Cyclotron (SSC). The facility is a multidisciplinary institute providing particle beams for physics research, particle therapy and radioisotope production [15]. Figure 2.1 shows the floor layout of the accelerator facility as well as the locations of the three particle accelerators.

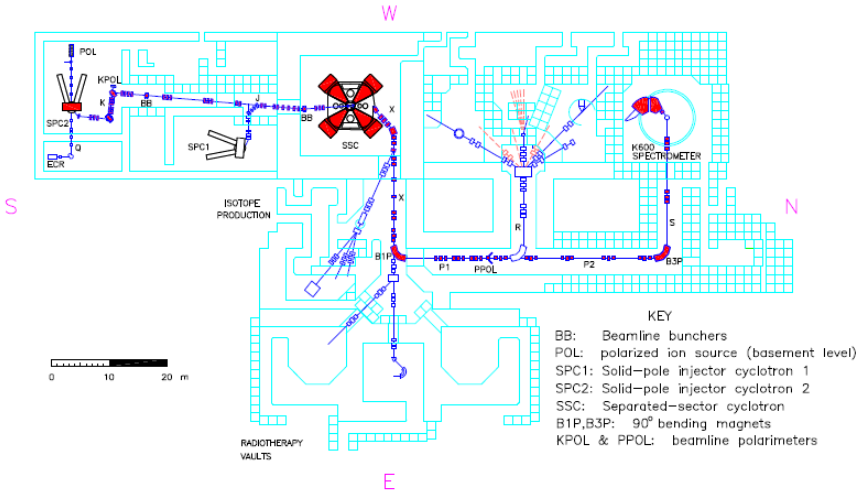

Figure 2.1: *The floor layout of the accelerator facility.*

For our experiment the required ^{4}He particle beam was produced in an Electron Cyclotron Resonance (ECR) ion source, situated below SPC2. All particle beams generated at the facility are pre-accelerated in one of the two injector cyclotrons, SPC1 or SPC2 [16]. They are capable of accelerating produced ions up to about 10 MeV and in our case to allow for the faint beam dispersion matching optimization technique, SPC2 was carefully chosen for beam pre-acceleration. To finally achieve the desired beam energy of 160 MeV, the beam was extracted from SPC2 through the K-section beam line for injection into the SSC. The beam energy of 160 MeV proved optimal for coincident scintillator triggering given that α particles coming off the reaction were stopped in the first paddle scintillator, with only a few high energy protons reaching the second paddle scintillator [17].

Positioned in the center of a 524 mm diameter scattering chamber, the L-shaped target ladder (made of Aluminum) can hold six different targets simultaneously. The target ladder was linked to a remote target-positioner, able to select different target frames by moving the ladder up or down, while being oriented perpendicularly to the direction of the beam (see Fig. 2.2). For the

scope of this experiment data was acquired using a 2.1 mg.cm^{-2} thick ^{24}Mg target foil. Other targets include ^{12}C of thickness 0.3 mg.cm^{-2} to investigate the existence of a possible 2^+ excitation of the 7.65 MeV 0^+ Hoyle State and a 2.1 mg.cm^{-2} thick ^{58}Ni target of which the data will be analyzed to further characterize the 1^- state at 6.026 MeV [18]. Furthermore, an empty frame similar in size to the ^{58}Ni target was used for beam-halo monitoring followed by viewers one and two consisting of fluorescent material used for beam spot optimization.

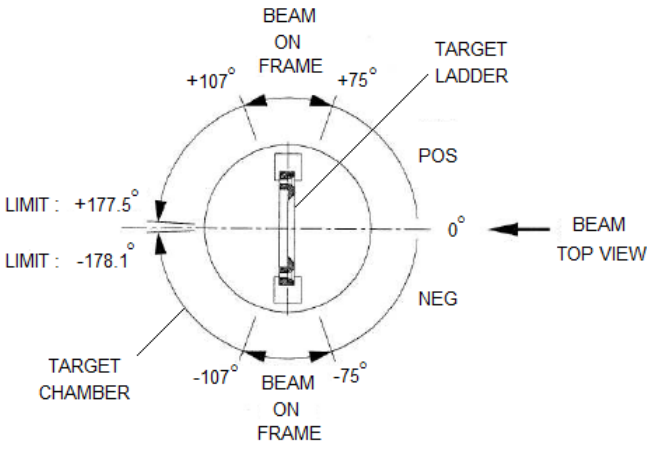

Figure 2.2: *Beam orientation on target chamber.*

2.2 The K=600 Magnetic Spectrometer

The combination of a magnetic spectrometer and an accelerator beam has over the years proven a powerful tool, offering information on nuclear structure as well as on nuclear reaction mechanisms of unprecedented quality. By achieving horizontal spatial separation of ejectiles characterized by their degree of ionization, different excited states within the target nucleus can be identified. This selectiveness property of a spectrometer, to be able to distinguish between particles of different momentum (energy) is often referred to as the magnetic rigidity R. The details of this concept are further discussed in section 2.2.1. However, as the need to venture further into nuclear structure arouse, it became evident that even higher still resolving power was necessary to separate dense nuclear states. This was realized with the advent of matching conditions for magnetic spectrometers [19]. The full capability of resolving power of a magnetic spectrometer can only be achieved if the characteristics of the beam coming from the accelerator are matched to those required by the spectrometer. Furthermore, these matching conditions are essential when performing zero-degree measurements, since particle flux is increased tenfold

hindering the ability to extract meaningful nuclear spectroscopic information against intense backgrounds.

The framework as well as the methodology behind operating the K600 in zero-degree dispersion matched mode is outlined in the sub-sections to follow. More specifically, they include key concepts such as dispersion matching with faint beam, transmission efficiency, background minimization, as well as the beam diagnostic techniques that accompany these methods.

2.2.1 Spectrometer Overview

The K600 magnetic spectrometer (see figure 2.3) is a high resolution detector system of which the three main optical components are a quadrupole (Q) and two dipole magnets (D1 and D2), i.e. a so called QDD configuration. The quadrupole magnet is used for focusing reaction products in a vertical direction while the dipole magnets are the main dispersion elements achieving spatial separation in the horizontal plane. Depending on the momentum range, the spectrometer can be operated in a low-, medium- or high-momentum dispersion mode, with the last mentioned being the one used in this study. As can be seen in figure 2.3, the different dispersion modes each have their corresponding focal planes positioned at the spectrometers exit. Two trim coils, the so-called H- and K-coils situated inside the dipoles D1 and D2 provides final focusing, compensating for kinematic corrections of reaction products at the focal plane. Specifically, the K-coil is used to adjust for first-order point-to-point position corrections as a function of the focal plane angle, while the H-coil adjusts for second order corrections. These are often referred to as correction of the $(x|\theta)$ and $(x|\theta^2)$ aberrations respectively [20]. The nature of these terms refer to the correlation of the focal plane position with respect to the scattering angle.

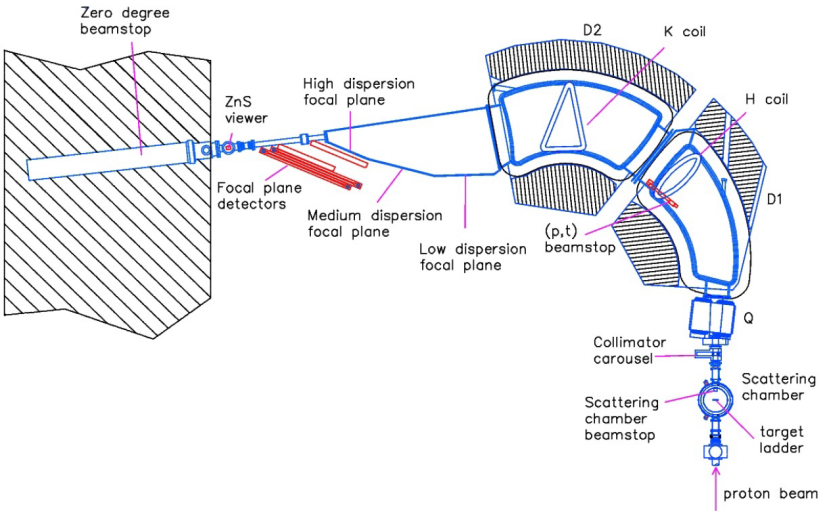

Figure 2.3: *Schematic view of the K=600 magnetic spectrometer.*

The scattered particles pass through a collimator, housed in a carousal situated in front of the quadrupole. The collimator carousal can hold six different collimators, and depending on which one is used, defines the angular acceptance of the spectrometer. Governed by the magnetic Lorentz force

$$\overrightarrow{F} = q\overrightarrow{v} \times \overrightarrow{B} \quad , \tag{2.2.1}$$

a charged particle entering the magnetic field of the spectrometer with velocity $\overrightarrow{v}$ and charge q experiences a force $\overrightarrow{F}$ proportional to the magnetic field strength. This force will guide the charged particles into a circular motion thus acting as a centripetal force. The path followed by a particle through the spectrometer is then curved according to the radius of curvature caused by the induced centripetal acceleration. This property is exploited by the spectrometer allowing the different species of particles to be distinguishable in the focal plane. Consequently, by comparing this magnetic Lorentz force and the general expression for a centripetal force we get

$$qvB = \frac{mv^2}{r} \Rightarrow rB = \frac{p}{q} \quad , \tag{2.2.2}$$

where m is the mass and p the corresponding momentum of the particle. Furthermore, we define the magnetic rigidity R of the particle as the quantity rB, i.e.

$$R = \frac{p}{q} \quad . \tag{2.2.3}$$

By taking the non-relativistic expression for the momentum of the particle, $\sqrt{2mE}$, the magnetic rigidity can be expressed as

$$R = \frac{\sqrt{2mE}}{q} = \sqrt{2K} \quad , \tag{2.2.4}$$

with K being the energy constant associated with a particular magnetic spectrometer [21]. Often referred to as the K-value, it denotes the maximum possible value of K, limited by the spectrometers design. From equation 2.2.4 it then follows that

$$K = \frac{mE}{q^2} \quad . \tag{2.2.5}$$

Thus particles can have the same magnetic rigidities i.e. the same K-value and therefore follow the same curved path through the spectrometer. These particles may however, have different masses, charges and energies but will ultimately end up on the same position in the focal plane [22].

The K= 600 magnetic spectrometer at iThemba LABS has a K-value of 600 i.e. it can detect protons or α particles up to a maximum kinetic energy of 600 MeV. For a particular momentum range (see table 2.1) and thus a specific magnetic field setting for the K600 based on the K-values for the particles of interest, we were able to look at a relatively narrow energy region in the focal plane. However, following the argument of focusing same K-valued particles at the focal plane, this translates into the possibility of detecting unwanted reaction products amongst the particles of interest. For a zero-degree measurement this undesired attribute is further enhanced, requiring a detailed analysis of the times taken by the vast range of detected particles to traverse the spectrometer, in order to characterize ejectiles successfully.

This time-of-flight (TOF) techniques together with the procedures to perform zero-degree measurements will be discussed in detail. A summary of the K600 spectrometers technical specifications for operating in the high dispersion mode is given in table 2.1.

Property	High dispersion focal plane
Max momentum per charge (MeV/c)	1005
Max proton energy (MeV)	437
Max magnetic rigidity (T-m)	3.50
Max dipole fields, D1/D2 (T)	1.64/1.23
Nominal bend radius (m)	2.1
Nominal bend angle (degrees)	115
Max solid angle $\Delta\theta\Delta\phi$ (msr)	6.0
Max radial acceptance $\Delta\theta$ (mrad)	$\pm$44
Max axial acceptance $\Delta\phi$ (mrad)	$\pm$44
Momentum range P_{max}/P_{min}	1.063
$p/\delta p$: Resolving power	?
$(x\|\frac{\Delta p}{p})$: Momentum dispersion (cm/%)	9.8
Energy dispersion (keV/mm)(for 160MeV alphas)	40
$(x\|x)$: Horizontal magnification at p_{max}	-0.68
$(y\|y)$: Vertical magnification at p_{max}	-11.8
$(\theta\|\theta)$:	$1/(x\|x)$
$(\phi\|\phi)$:	$1/(x\|x)$
Focal plane length, horizontal (cm)	62
Tilting of focal plane w.r.t. central ray	32.2°

Table 2.1: *Technical specifications for the high dispersion mode of the K600 Magnetic Spectrometer.*

2.2.2 Zero-Degree Mode

Operating the K600 in the zero-degree mode (i.e. the angle between the spectrometers entrance and the incident beam is 0°) presents a difficult experimental challenge in its own right, since it not only depends on beam delivery subject to stringent requirements but also demands that these conditions remain very stable to make meaningful measurement periods possible. During zero-degree measurements both the primary beam and scattered particles are transported through the spectrometer, with the beam passing only a few centimeters from the edge of the sensing region in the high dispersion focal plane. This allows us to reach lower excitation energies but with the undesired effect of increased background and sensitive beam halo conditions. Within the selected momentum range this translates into small differences in the magnetic rigidities between the projectiles and the scattered particles. Thus the sensitiv-

ity of measurements to beam stability, transmission efficiency and subsequent changes of the background are greatly enhanced.

Furthermore, to achieve high spatial resolution in the focal plane a dispersion matched beam with reduced halo conditions must be realized such that the particles of interest can be characterized by the spectrometer. Dispersion matching for the K600 is achieved via the faint beam technique and is largely centralized around methods such as lateral dispersion, focus matching and angular dispersion. This particular procedure as well as the details surrounding the unique issues characteristic to our experimental setup have clear guidelines and will be outlined thoroughly.

2.2.2.1 Dispersion Matching

To obtain the full high resolution detection capabilities of a magnetic spectrometer i.e. to extract good quality spectra from measurements in the focal plane detectors, it is important to match the beam characteristics at the target to those required by the spectrometer. The momentum (energy) spread, Δp, of the accelerated beam is directly proportional to the beam momentum (energy). Higher beam energies have the inherent quality of large momentum spread which significantly limits the resolution of measured momentum spectra.

The essence of focus matching, lateral and angular dispersion matching is to realize an achromatic focus and zero angular-dispersion condition in the focal plane. The ion-optical concept of matching conditions is illustrated in figure 2.4[19]. From figure 2.4 (a) for a beam not dispersion matched the trajectories of three central rays with corresponding momenta of

$$\delta_0 = 0, \pm\frac{\Delta p}{p} \quad , \tag{2.2.6}$$

are shown. With δ_0 being the spread of the beam, particles with different δ_0 values are momentum analyzed by the spectrometer. Thus for an achromatic beam focus at the target, a finite beam width corresponding to the beam momentum spread is caused in the focal plane. For a dispersion matched beam, monochromatic focus is achieved at the target. Consequently, rays with different δ_0 values are focused at different positions on the target. The dispersion in the beam is then compensated for and matched by the spectrometer to realize an achromatic focus in the focal plane. A typical trajectory of a dispersion matched beam is seen in figure 2.4 (b). However, large beam size required for lateral dispersion matching gives rise to ambiguities in the determining of

the scattering angle. Lateral dispersion matched rays traverse the focal plane detection setup at different incident angles making horizontal and vertical angle reconstruction challenging. Thus by choosing appropriate incident angles for beam rays with different δ_0-values at the target (refer to figure 2.4 (c)), particles scattered with the same effective scattering angle are expected to arrive at the focal plane with the same angle independent of the target location. Dispersion in the scattering angle is minimized allowing for accurate angle definition.

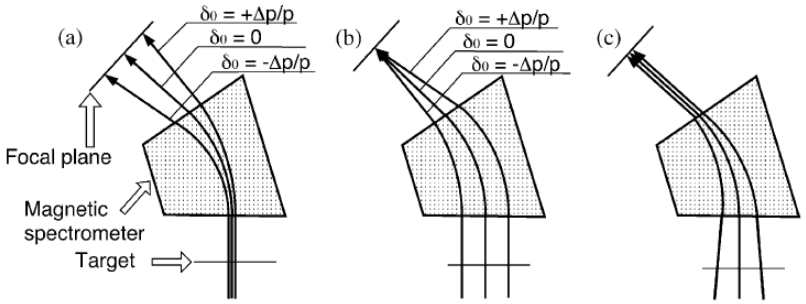

Figure 2.4: *Ion optical concept of dispersion matching conditions.*

The beam setup procedure for dispersion matching conditions at the iThemba LABS K600 facility, can be summarized as follows:

Firstly, we consider the whole accelerator and beam transport system as consisting of two main sections, namely, everything before slit 9X (i.e. the ion source, SPC2 and the SSC) and everything after (i.e. beamlines P1, P2 and S), referred to as the accelerator and high-energy beamline sections. Initially the accelerator and the beamline elements up to the object slit 9X (horizontal and vertical slits 9X illustrated in figure 2.1) must be tuned to deliver a high quality beam. For a zero-degree measurement this entails starting at a finite angle and optimizing the achromatic beam to ensure small beam E-spread and good halo conditions from the SSC. In turn these high quality beam conditions require single-turn extraction from the SPC2 and the SSC, which is achieved through a combination of relatively large orbit separation at extraction, low energy spread and small radial emittance. At this stage the measure of the quality of the beam translates into ensuring a small horizontal beam size at the object point as this is a necessary condition for high energy-resolution in the spectrometer focal plane [19]. Once all this is achieved the spectrometer can be moved to zero-degrees and the beam can be transported through the K600 (with the fluorescent beam viewer positioned on the target ladder incident to the beam) into the zero-degree beamline equipped with a Faraday cup embedded in the wall as seen in figure 2.3. The zero-degree beamline is

fitted with a scintillating viewer to assist with beam transmission through the spectrometer and characterization of the beam spot at the focal plane.

Beyond the object point, the X beamline as well as the P and S beamlines contains the main beam-tuning optical components necessary for dispersion matching. By optimizing these elements lateral dispersion and focus matching conditions are achieved between the beamline and the K600 magnetic spectrometer [23] [24]. Care should be taken in this respect to minimize the beam halo up to and at the object slits, without creating more halo downstream. At this point by observing the direct beam going into the spectrometer, matching conditions can be diagnosed accurately from the beam properties in the focal plane. However, even a beam as weak as a nA will damage the focal plane detector system during a measurement. Therefore, we make use of the faint beam method to realize dispersion matching. By positioning three beam attenuation meshes between the ECR ion source and SPC2 (refer to figure 2.1) the beam intensity is reduced by a factor of 10^6 particles/sec, without changing the emittance or the ion-optical characteristics of the beam. The dispersion matched faint beam is now measurable in the focal plane and is steered from the zero-degree beamline in the direction of the high dispersion focal plane, through scaling the five spectrometer magnetic elements by the same factor, i.e. magnetic elements D1 and D2, the K- and H-coils and the quadrupole. If dispersion matching is achieved, a beam image as illustrated in figure 2.5 is observed in the scatter plot. Optimization involves minimizing the size of this beam image to reproduce spectra with high-energy resolution.

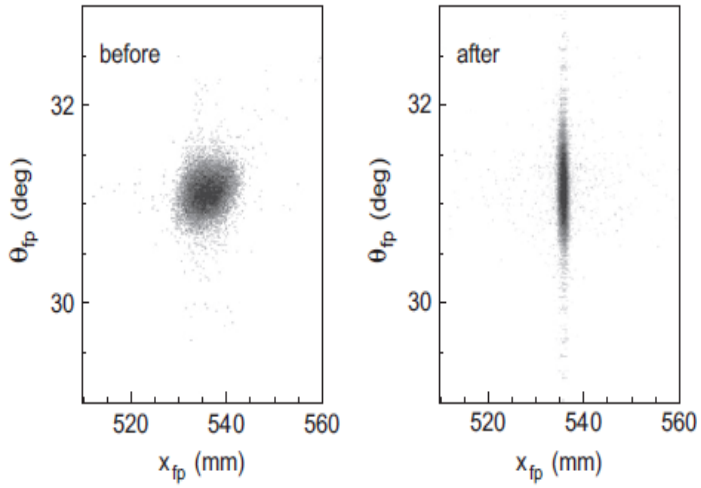

Figure 2.5: *The faint beam image in the (x_{fp}, y_{fp}) scatter plot before and after lateral dispersion and focus matching are achieved.*

Beam dispersion specifically required at the target of the K600 at iThemba LABS is relatively small, approximately 6 mm in width [14]. This is in comparison to similar dispersion matching spectrometer setups, such as the K=600 magnetic spectrometer at the Indiana University Cyclotron Facility (IUCF) and the Grand Raiden magnetic spectrometer at RNCP [25]. The beam-spot on target and the beam spread is therefore significantly reduced, resulting in a less severe angular dispersion mismatch. Together with offline analysis and lineshape corrections for spectra involving focal plane parameters, uncertainty in determining the horizontal scattering angle (θ_{scat}) is further minimized.

2.2.2.2 Transmission Efficiency and Background Reduction

One of the critical procedures of a zero-degree measurement is to ensure maximum beam transmission from the SSC up to and beyond the object slits in the X-, P- and S-beamlines and then eventually through the spectrometer. If only a very small fraction of the beam with typical currents of between 1 nA-2 nA touches any exposed elements in the beamline or the spectrometer, the background count-rate becomes increasingly large. The goal is to reduce this background count rate in the focal plane to $\sim$ 100 Hz at 1 nA, with an empty target using the direct beam going into the spectrometer at zero-degrees [26]. The beam tuning procedures involved to achieve maximum beam transmission, concerns the use of horizontal and vertical slits to define the size of the beam at the object point. Slit 9X situated in the X-beamline, typically have horizontal and vertical size openings of 1 mm and 2 mm respectively, while beam divergence is defined by the horizontal and vertical slits 12X positioned 3.5 m downstream of the object point. The result is that for a 200 MeV proton beam extracted from the SSC only 8% reaches the target. This significant beam intensity loss, especially at higher energies, can be attributed to the possible existence of multiple beam halo sources of which is detrimental to measurements particularly at very forward angles.

Beam halo as a result of slit scattering is the main contributor towards increased background. Thus to obtain the high energy-resolution necessary to extract meaningful results against intense backgrounds, a reduced beam halo together with background minimization techniques has to be employed. Normally, the horizontal and vertical slits 1P, 3P and 10P in the P-beamline are used as background reducing slits. Specifically, beam halo originating from small-angle slit-scattering are removed effectively by the energy definition slit 1P, while slits 3P and 10P mainly function as clean-up slits intercepting the majority of the remaining beam halo. In the S-beamline located at the focus point of the second symmetrical double-focusing bending magnet B3P, the horizontal and vertical slits 2S is the last and crucial clean-up slits.

Besides beam halo originating from beamline or spectrometer re-scattering,

another potential source of background is target thickness. Particles resulting from small-angle elastic scattering off the target foil, in turn re-scatters off any exposed parts within the spectrometer contributing further towards unwanted background. This background component increases in proportion to increasing target mass [27]. Therefore, in order to ensure a cleaner transmission through the spectrometer, a dipole ratio of R = 1.49 for the high dispersion mode rather than the design ratio of R = 1.33 was chosen. Furthermore, the increased dipole field ratio has the added advantage of increasing the dispersion from the design value of -9.8 to -10.9 cm/% and allowing for measurements at smaller excitation energies.

2.3 The Focal Plane Detector Setup

Reaction products with typical flight paths of 8 m from the target to the focal plane, were detected by means of a focal plane detector array positioned along the high-momentum dispersion focal plane at the exit window of the spectrometer (see Figure 2.3). The detector array consisted of two XU vertical drift chambers (VDC's), followed further downstream by a 1/4″ and 1/2″ plastic scintillation detectors (Paddle 1 and Paddle 2). The plastic scintillation detectors provided the trigger signals for registering focal plane events.

The XU configuration VDC is a relatively new multi-wire drift chamber setup. It was manufactured at iThemba LABS and installed at the K600 magnetic spectrometer with the main purpose to improve accuracy when determining the scattering angle, during 0° measurements. The functionality behind this so-called XU configuration is concerned with determining where along the XU wire planes, the particle crossed. Furthermore, the paddle detectors aid with particle identification but not by means of conventional $\Delta E - E$ or $\Delta E - \Delta E$ techniques. Rather, due to the fact that most of the reaction products are stopped within the first few millimeters of paddle 1, time of flight measurements together with the energy loss of particles in paddle 1, are used to identify reaction products.

2.3.1 XU Vertical Drift Chambers

Scattering angle definition depends largely on the reconstruction of particle tracks within the focal plane. Consequently, this requires the accurate reconstruction of both vertical as well as horizontal components of the particles flight path through the focal plane detector array. With this in mind, an XU signal-wire configuration was selected for the new VDC's. The X signal-wires are perpendicularly orientated to the scattering plane while the U signal-wires are angled at 50° in relation to the scattering plane.

As in the case of the original VDC's the new VDC X wire-plane consists of 198 gold-plated tungsten signal-wires, 20 μm in diameter, spaced 4 mm apart. Interspersed between these wires at equal distances are 199 field shaping wires made of 50 μm diameter gold-plated tungsten. Similarly the U wire-plane consists of 143 signal-wires and 144 field shaping wires, also spaced 4 mm apart. In addition there is 1 extra guard wire at both ends of both wire planes. These are made from 125 μm diameter Ni-Cr wires (80%/20%), and are necessary to reduce the electric field at the ends of the drift chambers, so as to prevent spontaneous discharge and reduce leakage currents. The X and U wire planes are then positioned between three 20 μm thick negative high voltage aluminium foils, each with a distance of 16 mm apart as shown in figure 2.6. The volume in the VDC chamber is filled with a gas mixture of 90% Ar and 10% CO_2 and sealed off from the environment by two 25 μm thick Mylar planes [14].

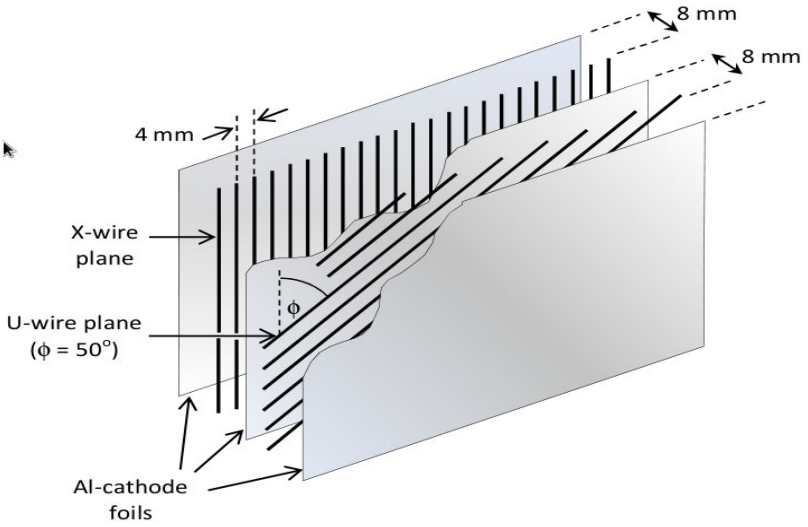

Figure 2.6: *Illustration of the XU multi-wire chamber, showing signal wire orientation and the Al-cathode planes.*

In a vertical drift chamber the drift direction of the electrons is perpendicular to the wire plane. Particles entering the chamber ionizes the Argon gas producing electrons that drift towards the nearest anode signal-wires (X-U planes), whereupon avalanching occurs. Negative high voltages of ~3500 V and ~500 V are applied to the cathode foils and guard wires respectively. Illustrated in Fig. 2.7, as a particle passes through the VDC at the trajectory angle for the central beam ray of 35.75°, 3-4 drift cells in the U-plane and 5-6 drift cells in the X-plane will record a charge. For the specific drift chamber used, drift distances of 8 mm can be expected corresponding to drift velocities and times of the order 4-6$\times$ 10^4 m.s^{-1} and 133-200 ns respectively [26]. Thus,

by making use of this drift time to drift distance mapping, together with the measurement of the time taken for electrons to drift from the primary point of ionization to the point where avalanching occurs, it is possible to accurately reconstruct the particles trajectory through the focal plane [26]. For a more detailed description regarding the XU drift chamber and their operation refer to references [28], [29] and [20].

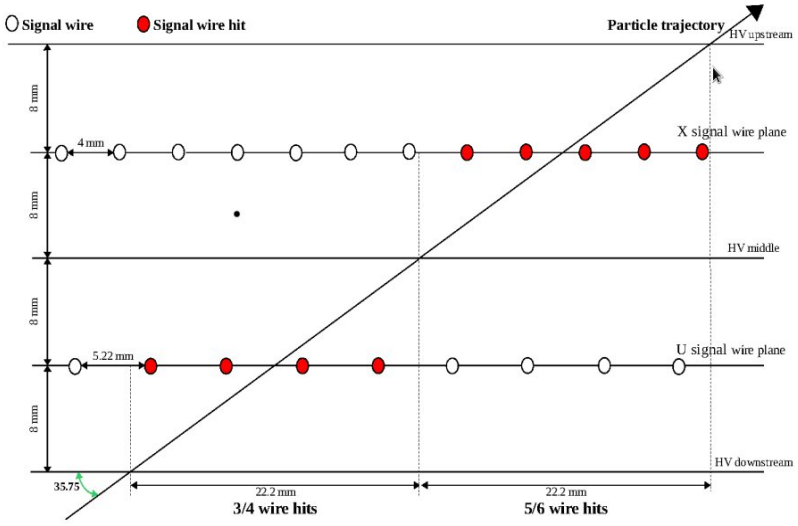

Figure 2.7: *View of a typical particle track passing through the XU wire chamber (excluding guard wires).*

2.3.2 Paddle Detectors

The two plastic scintillator detectors, referred to as paddle detectors because of their specific geometry, were positioned downstream behind the VDC's. The plastic scintillator directly behind the VDC's relative to particles traversing through the spectrometer is labeled paddle 1 with the scintillator that follows after that labeled paddle 2. The material used as the scintillating medium was BC-408, primarily because of its application in large area and time of flight (TOF) measurements [30]. The dimensions of the paddles are 122.0 cm $\times$ 10.2 cm and are coupled on both ends via light guides to photomultiplier tubes (PM-tubes) which are operated in coincidence mode. To prevent any interference from the surrounding environment, the assembled paddles were wrapped in aluminized mylar sheeting.

Used as trigger detectors, pulses from the paddle scintillators provide starting signals for time of flight measurements of particles traversing the spectrometer. Due to the incident energies of the inelastically scattered particles, most reaction products are stopped within millimeters in paddle 1, with only a few high energy protons reaching the second scintillator. With aid from the time

of flight measurements together with $\Delta E - \Delta E$ particle identification (PID) spectra, reaction products can successfully be labeled.

2.4 Ancillary Detectors

In the past the combination of γ spectroscopy with the inelastic scattering of α particles provided a powerful tool for the spectroscopy of low-lying nuclear excitations, with specific reference to the spectroscopy of the electric dipole (E1) strengths above and below the particle threshold. These investigations have become the renewed topic of interest due to the advancements in high energy resolution spectroscopy techniques and recent developments in the nature of these E1 transitions as a manifestation of a specific nuclear excitation mode, namely the so called Pygmy Dipole Resonance (PDR) (refer to refs. [6–8]). To fix the nature of the low-lying strength requires the identification of the isospin structure, and more specifically its isoscalar contribution towards the PDR. However, these approaches have made use of NaI scintillators to detect γ rays in coincidence with α's scattered by the target, thus limiting the application due to the poor resolving power of the NaI detectors which are unable to resolve the high density of levels in the excitation energy region of interest [5].

To obtain the high energy resolution required for the coincident measurement of γ-rays from nuclei excited in the reaction ^{24}Mg$(\alpha, \alpha'\gamma)$, two HPGe Clover detectors (Clover 1 and 2) as well as the HAGAR detector were placed at strategic backward angles around the reaction chamber. Positioned at $\theta_{lab} = 90°$ beam left and $\theta_{lab} = 147°$ beam right, Clover 1 and Clover 2 respectively, were operated in coincidence with the the focal plane detection setup to detect γ rays with specific α particle signatures, while the large NaI crystal from HAGAR was placed opposite Clover 1 at 90° beam right. The Clover detectors are four-fold segmented and compared to NaI detectors, have a lower intrinsic detection efficiency due to smaller detection crystal volumes as well as being a lower Z material. Consequently, to maximize the solid angle the Clover detectors were placed as close as possible to the target. For the HAGAR detector, the NaI crystal was coupled to a total of seven photomultiplier tubes and shielded by 8 plastic scintillation detectors situated on the circumference and extending the length of the NaI cylinder. Other critical issues include, the characterization of the gamma and neutron backgrounds as well as the investigation of the timing relation between the Clovers and the K600 focal plane detectors. The layout of the ancillary detectors are illustrated in Fig. 2.8.

Figure 2.8: *The experimental layout indicating the position of HAGAR and the two HPGe Clovers. In the top picture Clover 2 is shown together with HAGAR, with the beam direction from left to right. In the bottom picture Clover 1 is shown, positioned on the beam left.*

2.4.1 Add-Back and Photo-Peak Efficiency

The Clover detector is a detector assembly of four HPGe n-type crystals packed closely together, no more than 0.7 mm apart. The volume of a single HPGe crystal is 50 mm × 50 mm × 70 mm (total volume ± 4 × 50 mm × 50 mm × 70 mm) compared to the large NaI cylinder of radius 119 mm and length 356 mm [31]. Inherently, the Clovers have a much lower intrinsic efficiency. Thus to minimize this factor Clover 1 and 2 were positioned on the the edge of the reaction chamber housing ± 270 mm from the target subtending a solid angle of $\Omega = 0.105$ sr. The distance between HAGAR and the target was ap-

proximately 460 mm. All 4 crystals are held together on a crystal holder at the rear side of the detector housing, keeping the surrounding material within the detection region to a minimum. This improves the peak-to-background ratio but more importantly because of the very little absorbing material present, the full energy of a compton scattered photon detected in a second (or a third) crystal can be determined. This added feature is known as "add-back". The full energy peak of a photon is obtained by summing the energies deposited in the x-segments fired. Ultimately, the "add-back" efficiency is fourfold superior than that of the individual efficiencies, offering the desired high resolving power.

2.4.2 Clovers and K600 Focal Plane Timing

The measurement of γ rays from excited states requires a hardware coincidence between the focal plane and photon detection systems. More specifically, a coincidence between signals from the first plane of scintillators and any one of the Clover detectors is necessary for the main trigger to commence data acquisition. This in turn requires an alignment between the timing of the spectrometer and the HPGe Clover detectors. The signal processing of the Clover detectors is done with standard NIM electronics as outlined in section 2.9. Each Clover detectors preamplifier output is used to produce an energy signal and a fast timing signal. The signal is amplified and serves then as input into the CAEN V785 peak sensing ADC (Analog-to-digital converter) of the K600 DAQ. Here the energy signal is digitized by the 32 channel 12 bit ADC which forms part of the VME (Versa Modula Europa) output system of the K600. For the time signature each signal is processed by a TFA (Timing Filter Amplifier) and a CFD (Constant Fraction Discriminator). The outputs of the CFD's are fed into 32 channel TDC's (Time-to-Digital Converters) which uses the main trigger as a common stop, thus recording each signals time path.

The time difference between the α particle and the γ ray is a measure to distinguish between true and random coincidences. This being the most critical of the timing issues, relates to the fast timing nature of the HPGe Clover detectors in comparison to the time-of-flight (TOF) radio frequency (RF) of the SSC (Separated Sector Cyclotron). This translates into establishing that the timing of the γ-ray detection in the HPGe Clover detectors is significantly less than the RF period of the SSC such that the prompt peak corresponding to true coincidences is separable from the random periodical peaks of preceding and next beam bursts. A period of 77 ns between beam bursts is characteristic to our radio frequency of 13.0397 MHz and together with a timing resolution of 6 ns FWHM (subject to weekend one in-beam data) proved sufficient enough to prevent event mixing from different beam bursts.

2.4.3 Minimizing Neutron Damage

Further care was taken as to when the Clover detectors were installed in the K600 vault. To prevent them from further neutron damage, beam exposure had to be kept to a minimum. Consequently, they were only installed in the vault once all beam tuning procedures were completed and the beam was stable for longer than a few hours. There was a reported deterioration in energy resolution before and after beamtime, however it was agreed that it is not possible to determine whether this is a result of additional neutron damage during beam time. The two Clover detectors were in operation for a total beam-time of 56 h over the two weekends at an average beam-current of 0.6 pnA. Furthermore, typical count rates of 8 kHz with HAGAR (sum of 7 PM-tubes), 3 kHz for the Clovers (per detector, sum of 4 crystals) and 1 kHz for the K600 focal plane detectors were recorded.

2.5 Electronics

The electronic setup used for processing signals from the detector array in the K600 vault comprises of standard NIM (Nuclear Instrumentation module) modules and a VME-based (Versa Modula Europe) DAQ. Most of the electronics in this setup is located in the K600 vault together with the detector array and are shielded behind lead shielding. Specifically, signals from the VDC's and the paddles are processed in the spectrometer vault, while data acquisition dead time and beam current measurements can be performed from modules in the data room of iThemba LABS.

The block diagram outlining the signal logic used to process events registered by the spectrometers detectors is presented in Fig. 2.9. The output pulse associated with paddles 1 and 2 i.e. pulses from all four photomultiplier tubes, was fed into a linear fan-out channel (Lin Fan). For the two outputs coming from the Lin Fan associated with both paddles, one is fed into a current integrating Charge-to-Digital Converter (QDC) after a delay of 150 ns, while the other served as input to a constant fraction discriminator (CFD). The energy signals from the paddles are digitized by the QDC. A mean-timer between the signals from both photomultiplier tubes per paddle, allows for the extraction of a single signal independent of the interaction position within the plastic scintillator. The output from the mean timer then served as input to a four-fold logic unit (4FLU), after it was fed through a discriminator with a delay of 20.5 ns in the case of paddle 2. From the 4FLU, which is utilized to select paddle coincidence, the signal is split with one being sent to a second 4FLU upon which the RF signal is used as a stop trigger for the time-of-flight (TOF) Time-to-Digital Converter (TDC) to record a TOF measurement. The second output from the first 4FLU was sent to the TDC channels associated with the

VDC signals as well as serve as trigger for the ADC channels.

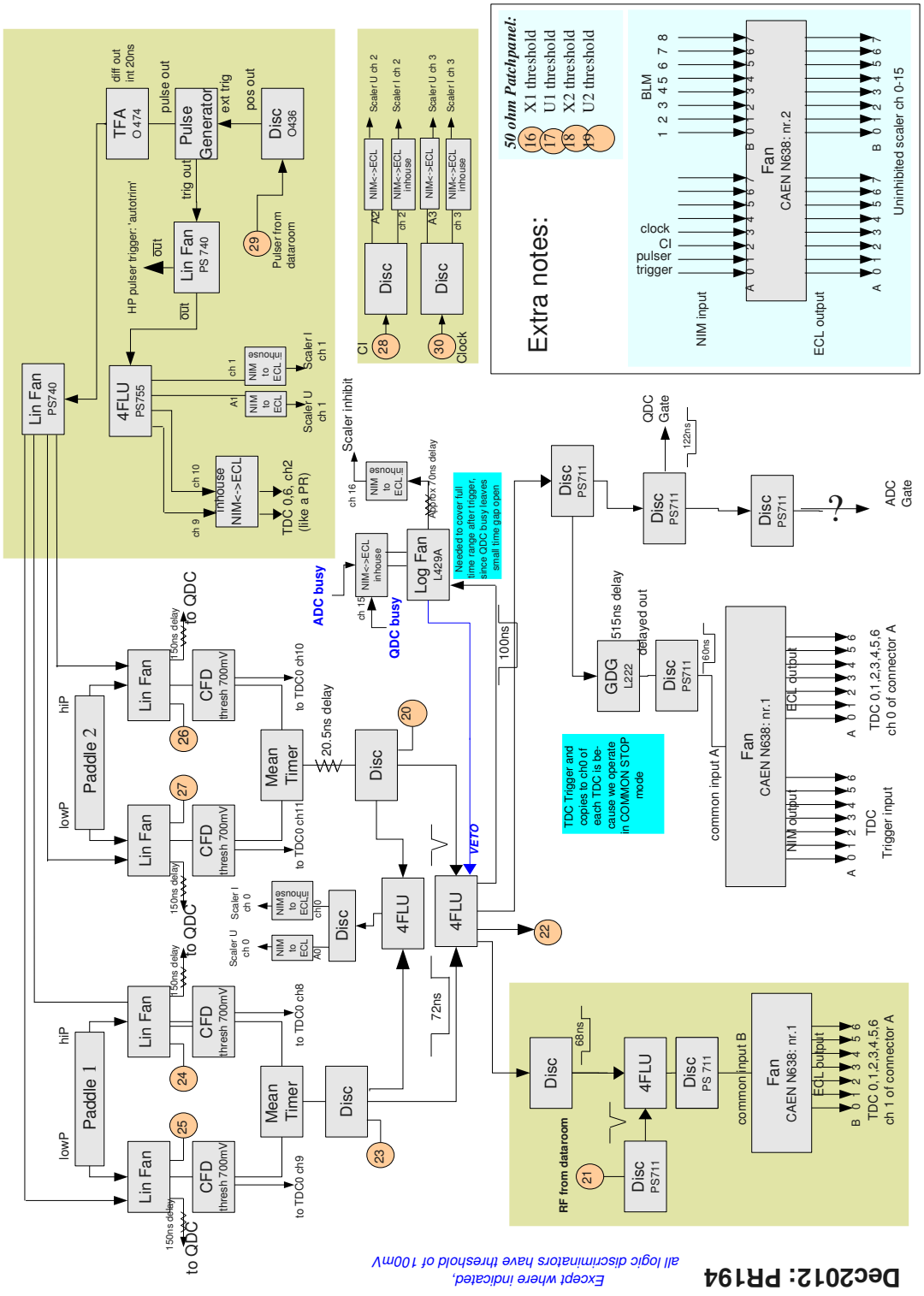

Figure 2.9: *Block diagram for the trigger logic.*

The signal wires from the drift chambers are connected to 16-channel pre-amplifier (pre-amp) cards. These pre-amps, besides amplifying the signals from the signal wires, perform a discriminatory function too ensuring that proper signals are sent to the TDC's. The drift times are measured by a 128-channel multihit TDC, connected to the pre-amps via 16-channel twisted pair ribbon cables. In total 13 pre-amps were used for the X-wire plane consisting of 198 signal wires, while 9 pre-amps were required for the U-wire plane consisting of 143 signal wires.

By comparing the amount of recorded inhibited and uninhibited pulses from two scalar modules, the effective dead time of the DAQ was measured. The two scalar modules were situated in the electronic setup where the pulser served as input. Furthermore, a Current Integrator unit (CI) measures the integrated current corrected for the DAQ dead time. A current reading at the beam stop is fed into the CI unit situated in the data room where at full-scale current the unit produces a pulse rate of 1 kHz. After being sent through a timing single channel analyzer (Timing SCA) to a discriminator, the output serves as input to a VME scalar module where together with the full-range setting the integrated current is calculated and corrected for the DAQ dead time.

2.6 Data Acquisition

Electronic signals were captured using VME-based hardware, performing the function of an interface between the electronics and the DAQ software. For online analysis signal processing is done by means of a network controlled data acquisition package called MIDAS (Maximum Integration Data Acquisition System), specifically used for nuclear and particle physics experiments [32]. Valuable features include a web interface allowing for experiments to be managed remotely as well as a fast online database.

2.7 Experimental Procedure

All electronics necessary for the general operation of the magnetic spectrometer was setup in the K600 vault, including those of the focal plane detection setup. With the focal plane detector array positioned at the high dispersion exit window of the spectrometer, the drift chambers were pumped down with gas to clear the sensing region of any contaminants. New to the existing setup was the installation of the γ-ray detectors for coincident photon decay. This included 2 HPGe Clover detectors and the Hagar NaI crytal as well as their accompanying electronics.

The experiment spanned two weekends, with weekend one being used to de-

velop the high energy resolution (α, α') capabilities at $\theta_{lab} = 0°$, while the second weekend was focused on the development of coincident γ detection.

2.7.1 Weekend 1

At the beginning of each weekend before the advent of the experiment, the basic procedures include pumping down the scattering chamber to the preferred vacuum, namely $\sim 10^{-5}$ mbar, after which the HV to the focal plane detector array is switched on. At this stage of weekend one the Clovers are not installed due to the potential neutron damage risk the beam tuning procedure poses. With the vault setup and ready to receive beam, the beam tuning procedure can begin (as outlined in section 2.2.2). For a finite spectrometer angle, to assist with aligning the beam on the target a fluorescent mesh, referred to as Hatanaka's mesh [26], as well as the ZnS viewers in the target ladder are used. The beam elements from the beam line is then matched to that required by the spectrometer in order to improve focal plane resolution. This dispersion matching procedure involves fine adjustments to both the currents of the quadrupole magnets as well as the horizontal and vertical beam slits situated in the high energy beam line. Once a beam with minimal energy spread and reduced halo conditions is achieved the spectrometer angle can be moved to 0°. The beam is then steered through the spectrometer and with reduced intensity (referred to as faint beam procedure, see section 2.2.2.1) via an adjustment of the spectrometers main magnetic currents, directed towards the high dispersion focal plane. This iterative procedure between dispersion matching and bean halo tuning is optimized to be able to make meaningful measurement periods possible, with optimal background conditions.

2.7.2 Weekend 2

When stable beam conditions are achieved, the HPGe Clover detectors as well as the HAGAR are installed in the K600 vault around the target chamber. For optimal functioning the Clover detectors should be kept at an ideal operating temperature, which means that the Clovers cooling tanks are to be checked and refilled with liquid nitrogen every 6-8 hours. Due to the sensitivity of the focal plane to beam halo and background, beam halo conditions are checked on a regular basis by characterizing the count rate in the focal plane. The goal is to maintain a background count rate of about 100 Hz at 1 nA with an empty target. With an optimally tuned beam and suitable magnet field settings for alpha detection, initial calibration runs are made. Data was taken for the beam on the ^{24}Mg target as well as on the targets ^{12}C and ^{58}Ni for 1 hour periods. The Clovers were utilized over the span of the two weekends for a total beam time of 56 h at an average beam current of 0.6 pnA.

Chapter 3

Data Analysis

During offline analysis the data acquired by means of the MIDAS data acquisition system for consecutive experimental runs were analyzed using a C++ based computer code called f-plane.c. The code reads in all TDC and QDC channel data, associates wire numbers with TDC channels and calculates the particle tracks through the wire plane. Developed at iThemba LABS, the code was written specifically with the new K600 focal-plane package in mind as well as to accommodate the extra ADC channels necessary for the gamma detectors. Within the different subroutines of the code, memory is first allocated to various histograms while the raw MIDAS event files are converted to ROOT tree data structures [33]. These *TTree* structures are defined for the important variables needed during data analysis, e.g. focal-plane position, time-of-flight (TOF), scattering angle, resolution, efficiency, etc. After satisfying a series of logical requirements the histograms are filled with the experimental data.

3.1 Particle Identification

3.1.1 Focal-Plane Particle Identification

Particle identification (PID) to isolate charged particles of interest in the magnetic spectrometer can be done by making use of two basic techniques. Governed by the Bethe-Bloch equation [34], method 1 is based on the fact that different particles lose different amounts of energy in a medium which is proportional to the velocity v and charge q

$$-\frac{dE}{dx} \propto \frac{q^2}{v^2} \quad . \tag{3.1.1}$$

The second method of particle identification relates to the interaction between

the charged particles and the magnetic field of the spectrometer (refer to section 2.2.1). Recalling equation 2.2.2 from section 2.2.1

$$qvB = \frac{mv^2}{r} \Rightarrow rB = \frac{p}{q} \quad , \tag{3.1.2}$$

we see that for a given reaction product with a characteristic momentum p, mass m and velocity v, it possesses a unique TOF range when traversing the spectrometers constant magnetic field B which is due to the particles radius of curvature r. Thus this implies that for a fixed magnetic field setting, a unique flightpath range will be assigned to each of the different types of reaction products.

In our experimental setup particle identification through TOF techniques translates into measuring the time elapsed between receiving an RF (radio frequency) signal from the SSC and registering an event in paddle 1. This is referred to as a relative TOF measurement. Thus the various loci visible in such a spectrum would indicate the different reaction products present in the focal plane. The alpha particles of interest can now be selected via a software gate on the corresponding TOF spectra, showing the energy deposited in paddle 1 as a function of the time-of-flight. Fig. 3.1 shows this selection of the alpha-particle distribution enclosed in a rectangular PID gate. Furthermore, these PID gates are used to generate position spectra like the example in Fig. 3.4 (see section 3.1.2).

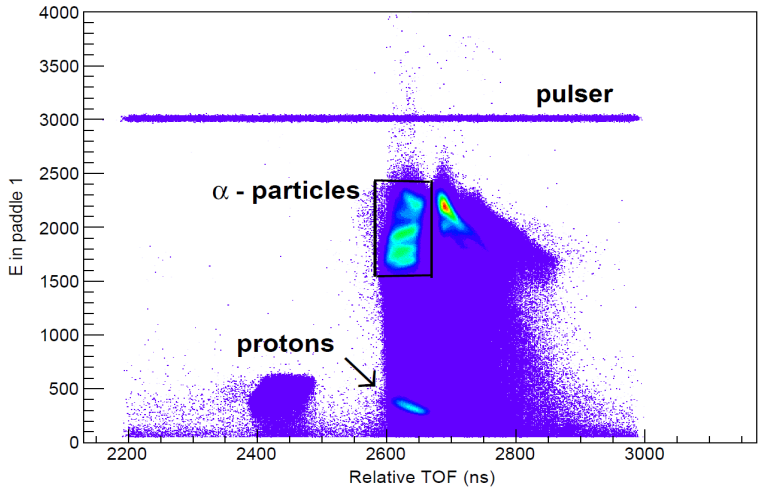

Figure 3.1: *A two dimensional PID spectrum of Paddle 1 vs relative TOF for the* $^{24}Mg(\alpha, \alpha'\gamma)$ *reaction. The rectangular software gate selects the alpha particles from the reaction products while other background from the pulsar and the high energy protons are identified too.*

3.1.2 Background Reduction

This being a zero-degree measurement, makes the experimental conditions very sensitive to background and thus a careful treatment of background reduction is necessary. Background reduction was optimized by characterizing the background in the various spectra of the focal plane parameters.

Beam related background constitutes an initial treatment. For the most part it can be attributed to the fact that the beam passes very close by the sensing region in the focal plane on its way to the zero-degree beamdump. With a comparison of a paddle 1 versus TOF spectrum for an empty target and one with a target, beam related background is clearly illustrated as seen in Fig. 3.2. Due to the clear separation of loci as discussed in the above section, most of the background is removable. Other related background can also be seen in this figure, such as the background due to the pulsar and some high energy protons, but can be removed via logic conditions during run analysis.

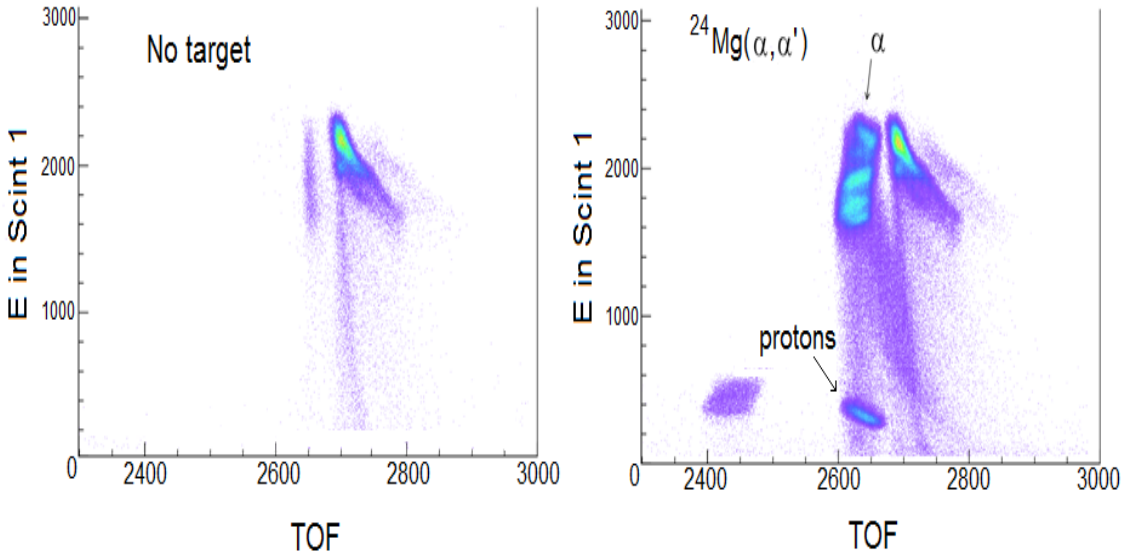

Figure 3.2: *A comparison of the measured Paddle 1 vs relative TOF spectra with and without a target reveals the subsequent background originating from the beam halo.*

A second treatment of background relates to identifying noise due to stray scattering. By inspection of the distribution of events in the vertical focal plane, we expect true correlated events to be sharply centralized around the vertical position Y = 0. The quadrupole magnet of the K600 is used in this sense to vertically focus the alpha particles of interest. These correlated events centered in the Y-direction are illustrated in Fig. 3.3 and are isolated by means of the dashed region.

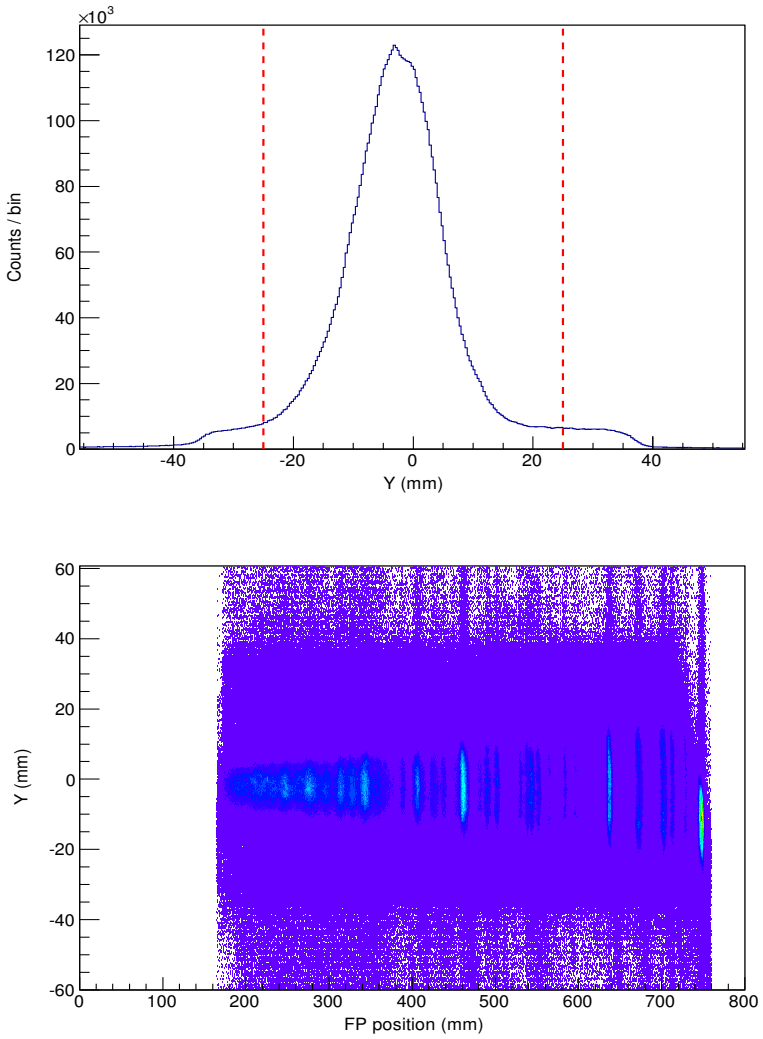

Figure 3.3: *The Y position and two-dimensional Y position vs X position spectra with the gated region representing true correlated events, marked out by the dashed lines.*

With the above mentioned treatment of background implemented, the scattering angle versus FP position two-dimensional spectrum and the corresponding FP position (horizontal X-position) spectrum is presented in Fig. 3.4. Distinct states are clearly visible as vertical loci in the two-dimensional spectrum. This approach to the treatment of background allows us to extract an almost background free X-position spectrum with the individual states clearly resolved.

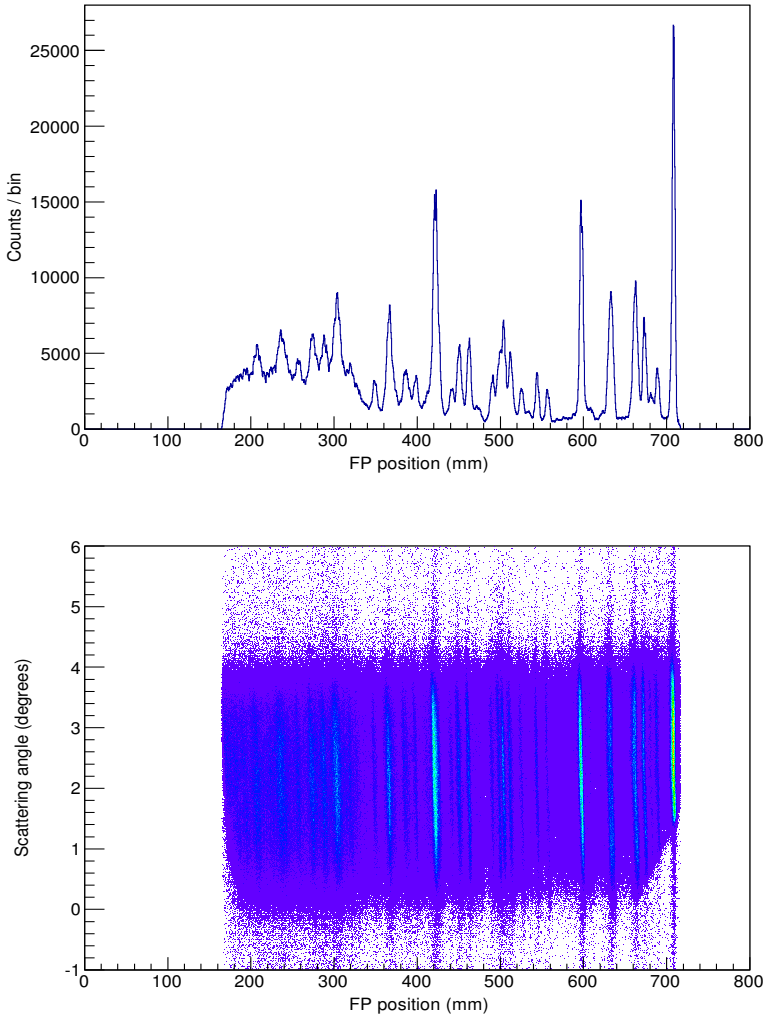

Figure 3.4: *FP position and the two-dimensional Scattering angle vs FP position spectra with individual states clearly resolved.*

3.2 VDC Operation

The position in the focal plane for a valid VDC event is determined by making use of the measured drift times and wire positions for each event. A drift time is defined as the time measured between the moment of initial ionization to the moment where avalanching takes place in each drift cell. Together with the known average drift velocities these drift times are then converted to drift distances, which is depicted here as the distance between the signal wire and the trajectory of the particle through the drift cell (see Fig. 3.7). Average drift velocities are characteristic to the VDC. The aim is then to directly link drift

distances to drift times by constructing a so-called lookup table (LUT) and consequently determining the focal plane coordinates for all valid VDC events. Section 3.2.4 outlines the requirements for the validation of VDC events.

3.2.1 Calculation of Focal Plane Coordinates

Reaction products that uniformly illuminate the whole focal plane and thus the VDC can be used to obtain the average timing response of all signal wires. This average of the resulting drift times for all signal wires makes up what is referred to as a "white spectrum". A typical "white spectrum"is shown in Fig. 3.5. The large peak to the right in the spectrum is associated with relatively short drift times due to cascading events that are situated near the signal wires. The flat region can be related to electrons of uniform drift velocity. Consequently, Fig. 3.5 depicts the counts per time bin, $\frac{dN}{dt}$, as a function of the time bin. Hence, once the characteristic drift-time distribution $\frac{dN}{dt}$ is known, it is possible to determine the drift distances of the electrons for each signal wire via the equation

$$x(t) = \left(\frac{dN}{dx}\right)^{-1} \int_{t_0}^{t} \left(\frac{dN}{dt'}\right) dt' \quad , \tag{3.2.1}$$

where t_0 is the initial time the particle strikes the drift cell, t is the time at which the anode registers a pulse and $\frac{dN}{dx}$ is the spatial distribution of events in the drift cell. Furthermore, due to the uniformity of the spatial distribution it follows that the time distribution $\frac{dN}{dt}$ is proportional to the average drift velocity

$$\frac{dN}{dt} \propto v(t) \quad . \tag{3.2.2}$$

Thus via equation 3.2.1, the lookup table is constructed by means of the so-called time-integral-spectrum method [35]. Fig. 3.6 illustrates a typical lookup table derived from a "white spectrum".

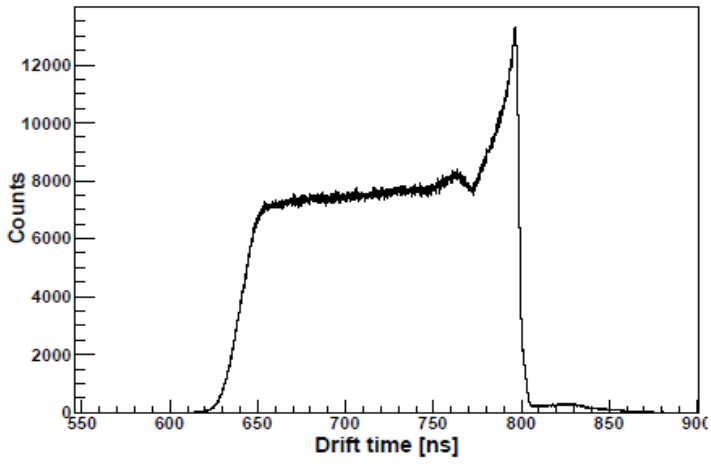

Figure 3.5: *A drift time measurement depicting a "white spectrum".*

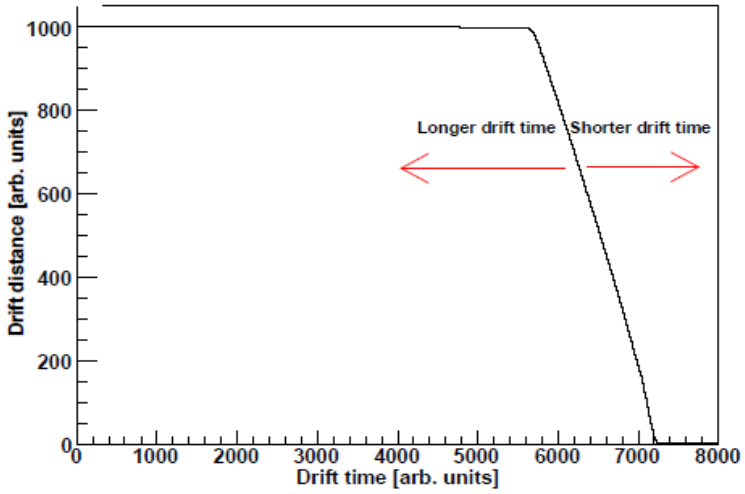

Figure 3.6: *Typical lookup table derived from a "white spectrum".*

3.2.2 VDC Spatial Resolution

For a particular set of drift distances and drift times, the position resolution of the VDC can be estimated as depicted in the following equation

$$\Delta = \frac{\mid d_{i+1} - d_{i-1} \mid}{2 - d_i} \quad . \tag{3.2.3}$$

Consider the wire-plane section in Fig. 3.7, where d_i and d_{i+1} are the drift distances for consecutive wires i and $i+1$. Ideally the position-resolution quantity, Δ, for a measurement would be zero. However, due to uncertainties in the drift-length measurements, we obtain a uniform distribution for Δ around zero. This translates into non-zero values for Δ and consequently, a decreased accuracy in drift time measurement.

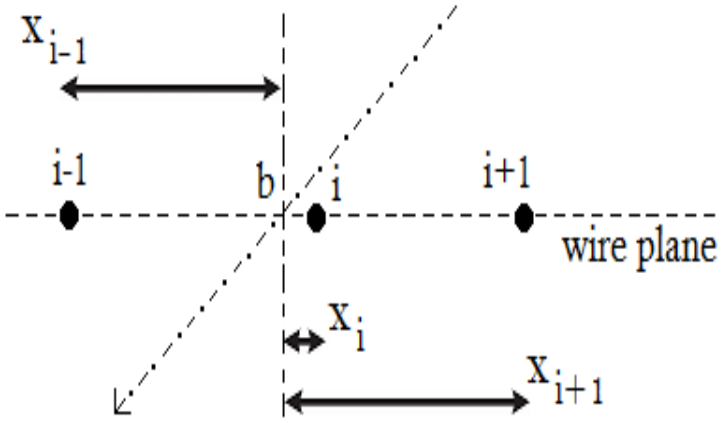

Figure 3.7: *Particle trajectory through the wire plane depicting the consecutive i-1, i and i+1 wires.*

3.2.3 Spatial Resolution Optimization

The spatial resolution calculated for the VDC can be optimized by a shifting in the lookup table. This is necessary due to the fact that it is nearly impossible to measure entirely accurate drift times, since delays in the the trigger signal commencing drift time measurements is unavoidable. Inaccurate drift times translates into incorrect drift distances recorded in the lookup table. For optimum resolution a one-dimensional plot of Δ, as described in the above section, should be sharply centered around $\Delta = 0$. Fig. 3.8 depicts this with a corresponding two-dimensional spectrum of Δ versus (b-integer(b)), where the variable (b-integer(b)) is depicted as the distance between the signal wire and the position at which the particle crossed the wire plane (see Fig. 3.7).

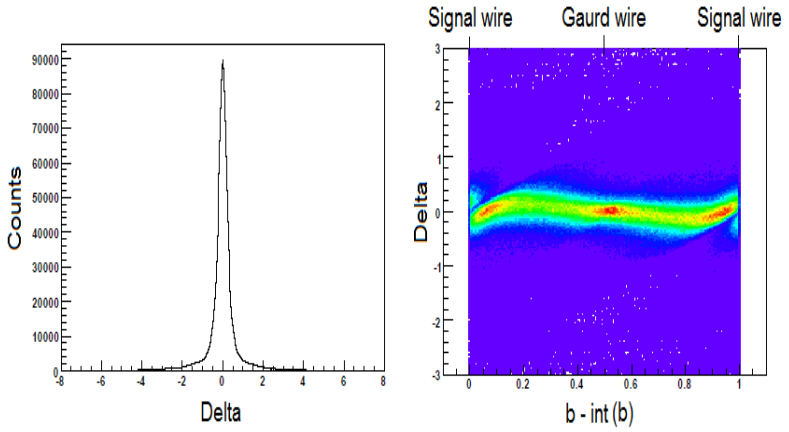

Figure 3.8: *Position resolution plot of* Δ *and a 2D spectrum of the projection of* Δ *on (b-integer(b)).*

3.2.4 VDC Efficiency

The VDC efficiency ϵ is related to the ability of the VDC to detect charged particles crossing the focal plane. Fig. 3.9 shows the measured raw wire hits per channel. From all these wire hits, valid events were selected to calculate VDC efficiency and later used to generate excitation spectra. The efficiency for the VDC wire chamber can be obtained by calculating the ratio of valid events to all PID selected events from the spectrum showing paddle 1 energy deposition as a function of TOF (see section 3.1.1). Following this argument, for measurements made with two drift chambers containing both X and U-wire planes the VDC efficiency can be calculated with

$$\epsilon_{X1X2U1U2} = X1_{\mathit{eff}} \times X2_{\mathit{eff}} \times U1_{\mathit{eff}} \times U2_{\mathit{eff}} \quad , \tag{3.2.4}$$

where Xi_{eff} and Ui_{eff} are defined here as the individual efficiencies of each wire plane (i = 1, 2) [36]. Xi_{eff} and Ui_{eff} are further denoted in terms of the valid events as

$$Xi_{\mathit{eff}} = \frac{Xi_{valid}}{Xi_{all}} \quad , \tag{3.2.5}$$

with a valid event being subject to the following requirements:

- at least 3 but not more than 9 signal wires must have registered a signal,
- drift times associated with these fired signal wires must fall within a specified range defined here by the drift time spectrum (see Fig. 3.5),
- and sets of fired signal wires should be successive, unless a maximum of one signal wire is missing in the adjoining set.

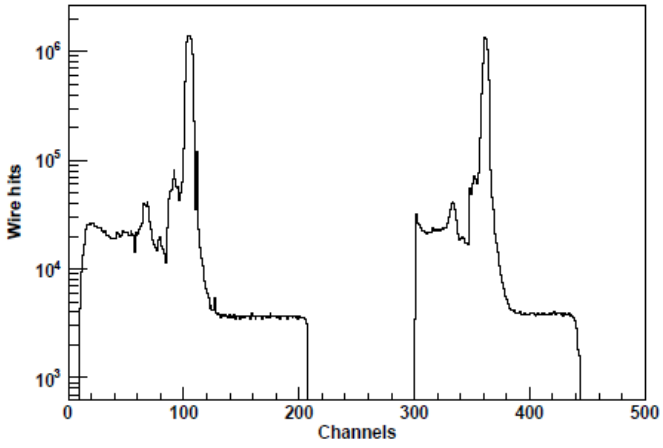

Figure 3.9: *The raw wire hits are shown per channel for both the X- and U-wire planes.*

The requirements for valid VDC events are coded into a subroutine located in f-plane.c, whereby all signal-wire events are sifted through to identify valid ones.

3.3 Energy Calibration

3.3.1 HAGAR Detector

The big NaI crystal from HAGAR to detect coincident γ rays from the $(\alpha, \alpha'\gamma)$ reaction, was calibrated using in-beam data. Since the HAGAR consists of a large NaI crystal connected to six active photomutliplier tubes (PM-tubes), calibration entails obtaining gains and offsets for each PM-tube independently. This involves the construction of a two-dimensional coincidence matrix of raw gamma energy per PM-tube versus excitation energy (refer to section 3.3.3 on excitation energy conversion). By selecting certain states within the excitation spectra and projecting onto the raw gamma-energy axis (Y-axis), gamma

transitions from these excited states are isolated and visible. Thus with the knowledge of the excited state selected, a calculated assumption can be made as to what γ rays are visible in the projection, based on the known γ rays originating from that particular state. Fig. 3.10 presents such a two-dimensional gamma energy versus excitation energy matrix for one of the six active PM-tubes.

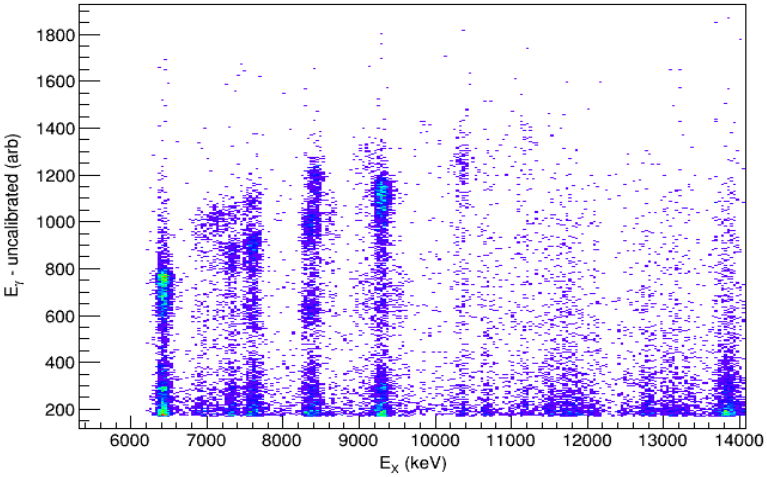

Figure 3.10: *The two-dimensional raw gamma energy for a single PM-tube from HAGAR versus excitation energy zoomed in for excitation energy between 5000 keV - 14 000 keV. Raw gamma energy referred to here represents measured gamma energy not calibrated.*

Excitation energy in the above spectrum is subject to all PID gates described in section 3.1, to obtain clean excitation spectra with minimal background which aids the gamma identification process during calibration. A projection onto γ-ray energy is illustrated in Fig. 3.11 for a selection of the 6432-keV excited state of ^{24}Mg. The projection gate on the 6432-keV state is visible in the region cut out by the two dashed lines. Table 3.1 shows all the prominent γ rays originating from the 6432-keV state of ^{24}Mg and based on this [39], the centroids of the gamma transitions in the projection are matched up to the known energies.

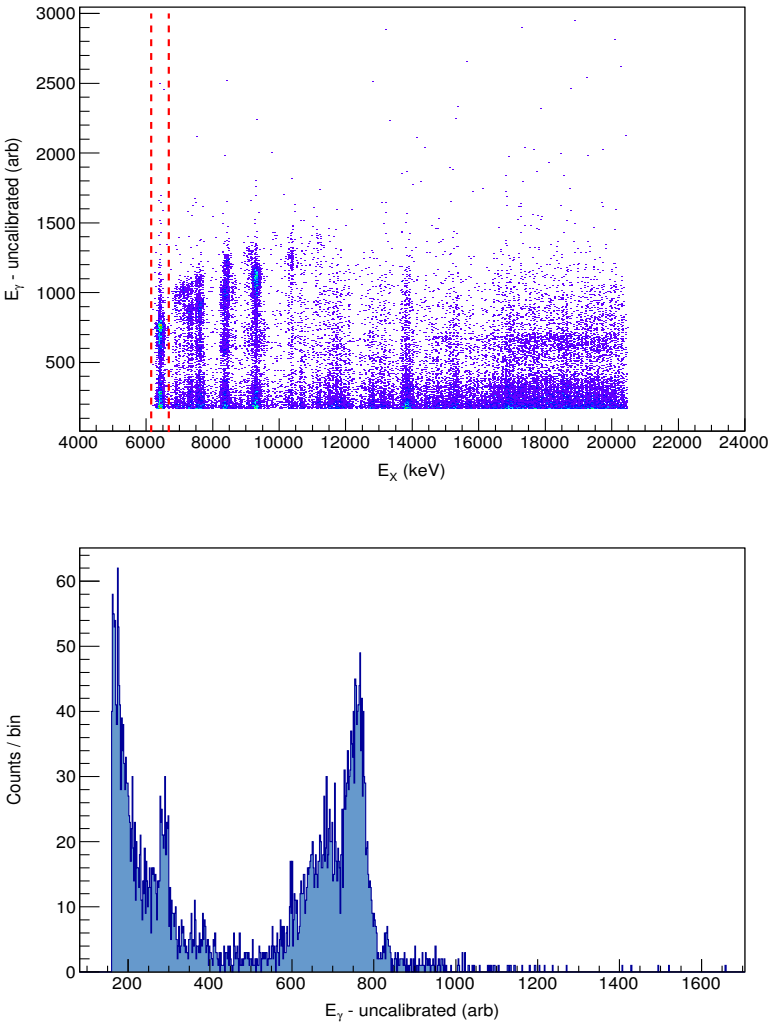

Figure 3.11: *The two-dimensional raw gamma energy for a single PM-tube from HAGAR versus excitation energy, with the gated region on the 6432-keV state representing the projection onto the decay-energy axis.*

Experimental value [keV]	Channel number (centroid)
1368	288.33
2193	391.61
5063	750.90

Table 3.1: *The known experimental γ-ray energy values in the first column are matched to the positions of the centroids of the peaks visible in the projection.*

The calibration was performed by assuming a linear relation between channel number and known γ-ray energy for the calibration points in Table 3.1. Fig. 3.12 illustrates this calibration curve.

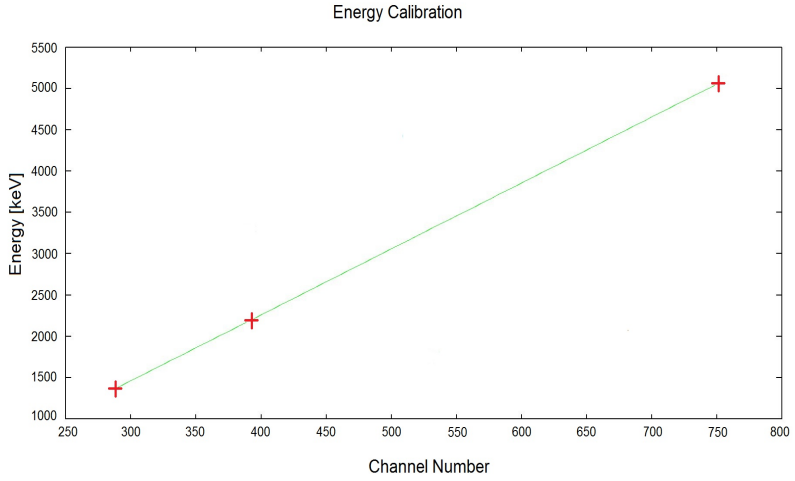

Figure 3.12: *Using Table 3.1 the calibration curve was obtained illustrating the linearity between known γ-ray energy and centroid position.*

The result obtained for the calibration of a single PM-tube was:

$$E_\gamma(\text{keV}) = (7.98799 \times \text{ADC}) - 935.187 \quad . \tag{3.3.1}$$

This procedure was followed for all six active PM-tubes with the calibration data summarized in Table 3.2.

PM-tube	Gain	Offset
1	7.98799	-935.187
2	9.11705	-1246.65
3	9.52288	-1172.71
4	9.34488	-1148.2
5	8.79776	-953.614
6	9.40119	-1092.56

Table 3.2: *The calibration information for all six active PM-tubes of the HAGAR detector.*

3.3.2 HPGe Clover Detectors

Calibration for the two Clover detectors is achieved by implementing the same procedure followed to calibrate the HAGAR detector. Since each Clover detector is fourfold segmented, the two-dimensional coincidence matrices are generated by plotting the raw gamma energy per diode per detector versus excitation energy. Thus when projecting onto raw gamma energy through the selection of certain states within the target nucleus, gamma-energy calibration information per Clover diode is obtained. A two-dimensional coincidence matrix for one of the diodes of a single Clover detector is shown in Fig. 3.13. Again selecting the 6432-keV excited state in ^{24}Mg and projecting onto the raw gamma energy axis, yields the gamma energy spectrum in Fig. 3.14.

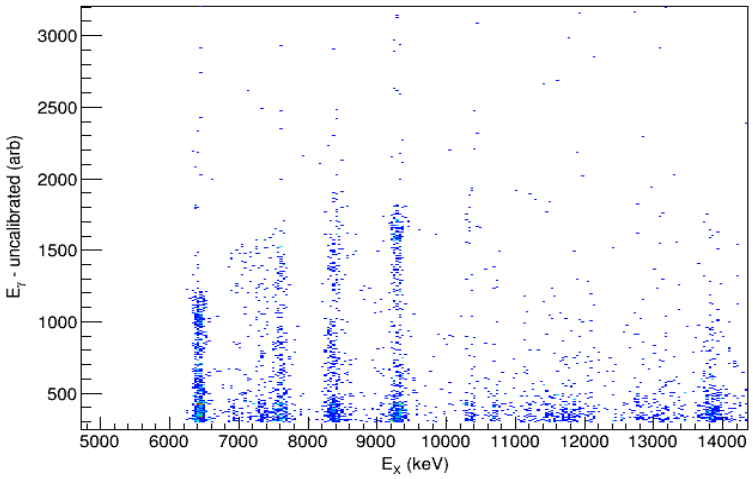

Figure 3.13: *The two-dimensional spectrum of raw γ-ray energy for one diode of a single Clover detector versus excitation energy zoomed in for excitation energy between 5000 keV - 14 000 keV.*

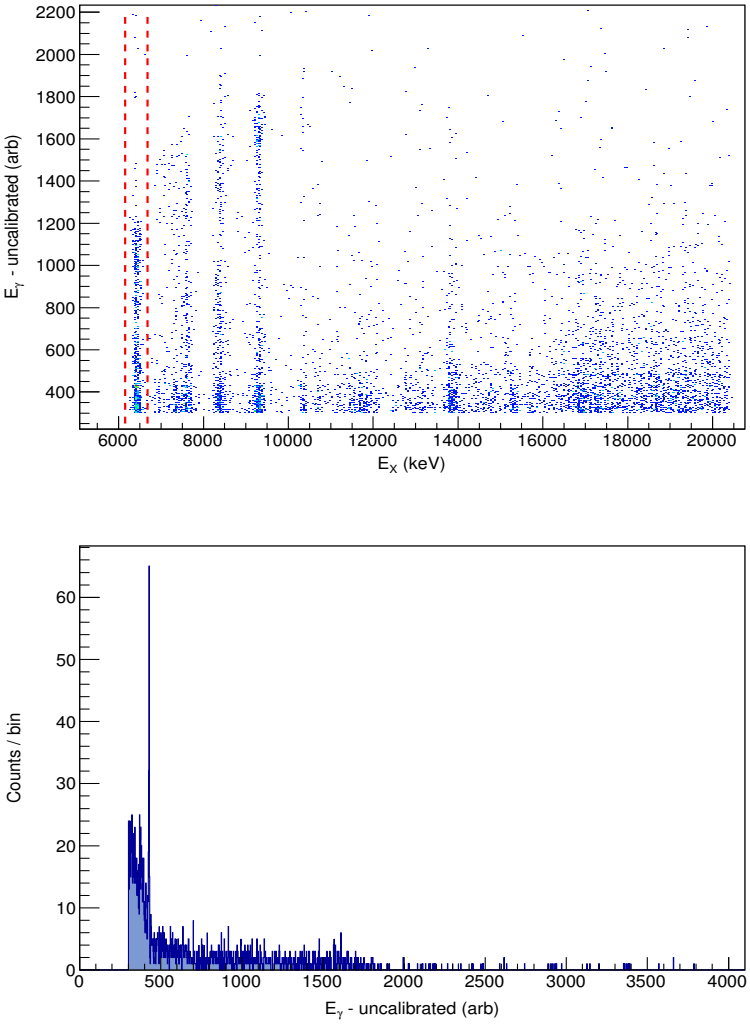

Figure 3.14: *The two-dimensional spectrum of raw γ-ray energy for one diode of a single Clover detector versus excitation energy, with the gated region on the 6432-keV state representing the projection onto the decay-energy axis.*

Using the same assumptions as in the previous section to identify gamma transitions from the 6432-keV state, we obtain the following calibration results for a single Clover diode:

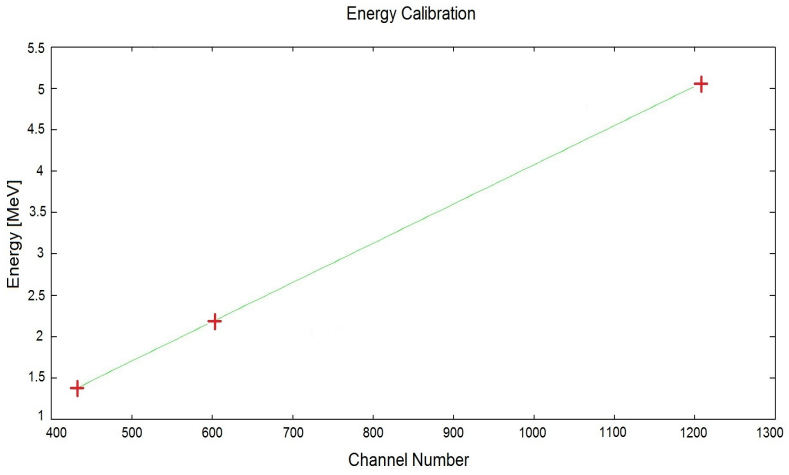

Figure 3.15: *The calibration curve was obtained using the known experimental γ-ray energies for the 6432-keV state in ^{24}Mg from Table 3.1 and the centroid positions of the visible peaks in the raw gamma-energy projection (Fig. 3.14).*

The following calibration relationship between γ-ray energy and channel number was obtained for the single Clover diode:

$$E_\gamma(\text{MeV}) = (0.0047450 \times \text{ADC}) - 0.664321 \quad . \tag{3.3.2}$$

The remaining 7 diodes from both Clover detectors were calibrated in the same way and summarized in Table 3.3.

Clover Diode	Gain	Offset
Clover1(a)	0.0047450	-0.664321
Clover1(b)	0.0044951	-0.6179
Clover1(c)	0.0045365	-0.6484
Clover1(d)	0.0037823	-0.5685
Clover2(a)	0.0048143	-0.6174
Clover2(b)	0.0041662	-0.5547
Clover2(c)	0.0039851	-0.4922
Clover2(d)	0.0034574	-0.4067

Table 3.3: *The calibration information of all eight diodes for both Clover detectors.*

3.3.3 K600 Magnetic Spectrometer

The K600 magnetic spectrometer was calibrated by means of the secondary α-beam elastically scattered from the ^{24}Mg target. This being a zero-degree measurement coupled with the high energy resolution capabilities, allows for visible nuclear states within the target to be well resolved. This is clear in the excitation spectrum Fig. 3.17 which is subject to the PID selected alpha particles being projected onto the focal plane position. Here particles with different momenta are magnetically analyzed and end up at different positions within the focal plane. The full scattering angle range, θ_{k600} = -1.91° to θ_{k600} = 1.91°, corresponds to an 800-mm focal plane range. Moving from right to left in focal plane position, excitation energy decreases.

From the above position spectrum the three prominent states in ^{24}Mg, as shown in table 3.4, are easily identifiable by way of the relative peak positions and by the line shapes of these peaks in spectra such as θ_{lab} vs X focal-plane position. The aim is to convert from focal plane position to excitation energy using a simple second order polynomial parameterized by the known experimental energy levels of the states within the target and the focal plane positions. Based on these assumptions, the outline for this procedure is as follows:

For the known energy states and their corresponding peak positions featured in Table 3.4, there exists a quadratic relationship between the momentum and the focal plane position. A fit between these two parameters together with the relation between α-energy E_a, momentum P and the mass of the particle m

$$E_a = \sqrt{(m^2)c^4 + (P^2)c^2} - mc^2 \quad , \tag{3.3.3}$$

provides us with a manner to calculate α energy, E_a, at any focal-plane position. We now convert E_a to excitation energy, E_x, for ^{24}Mg via the equation for the two-body reaction

$$E_\mathrm{x} = E_p + m_T - E_a - E_r \quad . \tag{3.3.4}$$

In the above equation E_p denotes the total energy belonging to the projectile, m_T is the mass of the target nucleus, E_a is the total energy of the ejectile and E_r is the total energy of the residual target nucleus [36]. Furthermore, residual target-nucleus energy can be calculated [37] by the expression

$$E_r = \sqrt{((P_0)^2 + (P_2)^2 - 2.P_0.P_2.\cos(\theta) + (m_3)^2)} \quad . \tag{3.3.5}$$

In Eq. 3.3.5 the indices 1-4 refer to the different particles, namely, the projectile, target, ejectile and recoil particles respectively. Finally, the quadratic relation between excitation energy, E_x, and horizontal focal-plane position X_{pos} is seen in Fig. 3.16 with the accompanying calibration formula

$$E_x(\text{MeV}) = (3.15436 \times 10^{-}3)X_{pos}^2 + (-0.012765)X_{pos} + 8.5432 \quad . \tag{3.3.6}$$

Experimental ^{24}Mg Energy Levels [keV]	Focal Plane Position [mm]	J^π
6432	712	0^+
9305	598	0^+
13850	345	-

Table 3.4: *The calibration information for excitation energy.*

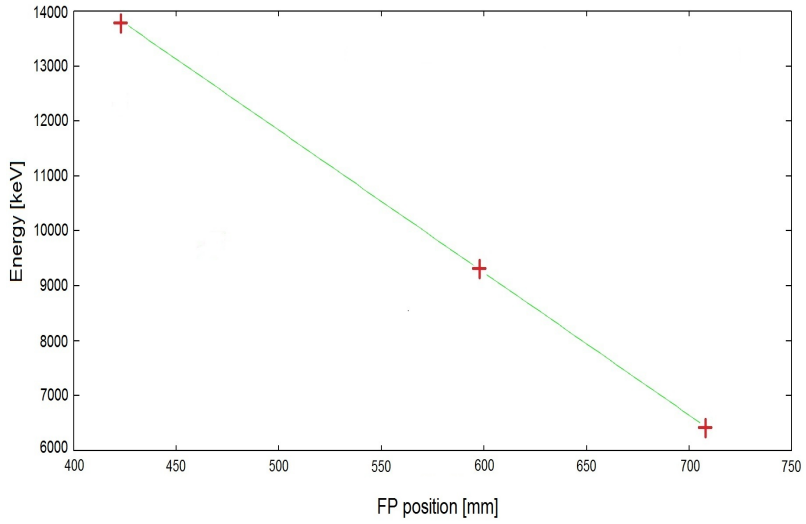

Figure 3.16: *This calibration curve was plotted for the ^{24}Mg spectrum with horizontal focal-plane position (X position) on the x-axis and experimental excitation energy values on the y-axis.*

Thus an excitation-energy spectrum for the ^{24}Mg target is presented in Fig. 3.17 using Eq. 3.3.6 for the various states identified.

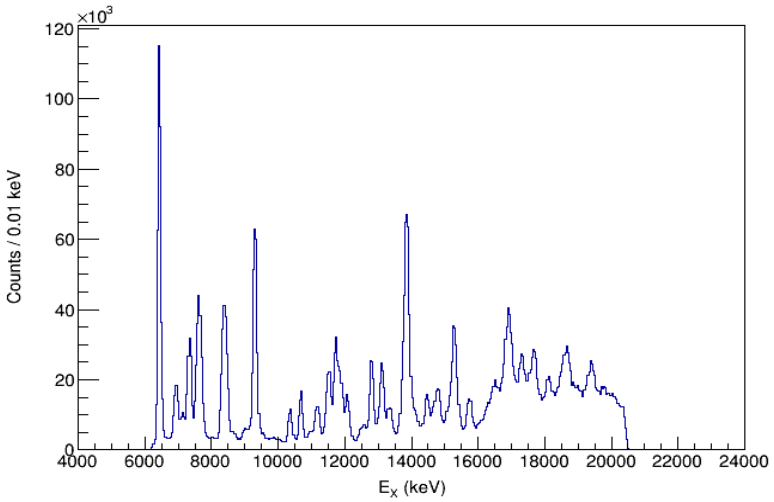

Figure 3.17: *Excitation-energy spectrum for the* ^{24}*Mg target.*

3.4 α-γ Coincidence Matrix

As seen in the previous section for the purpose of energy calibration, from the raw data a two-dimensional α-γ coincidence matrix is constructed. This is achieved through the combination of the excitation energy, deduced from the measured energy of the inelastically scattered α particles versus the γ-decay energy deduced from the energy of the emitted γ ray. These matrices are subject to several constraints and data reductions to produce spectra from which the cross sectional data for the excitation of single states can be extracted.

Fig. 3.18 represents the time spectrum for one of the Clover detectors with respect to the RF signal. The timing resolution in this spectrum is sufficient enough to separate the prompt peak from the smaller periodic peaks, present due to the preceding and next beam bursts. This large peak corresponds to true as well as random coincidences for which the α-γ coincidence originates from the same beam burst. Thus via a narrow cut on the prompt peak for each Clover TDC spectrum, random coincidences not originating from the same beam burst can be excluded from the data.

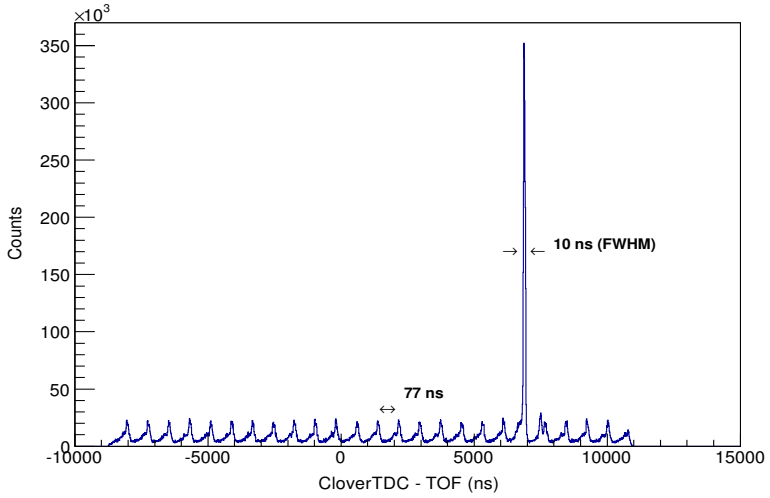

Figure 3.18: *The time difference between the γ detection and the TOF RF-signal for a single Clover diode. The timing resolution is 10 ns with beam bursts repeating every 77 ns. The prompt-to-random ratio is 3.5:1.*

The coincidence matrix is subject to additional data reductions as discussed in section 3.1.2, to further suppress background events. In the resulting matrix transitions between bound nuclear states appear as thin horizontal lines due to the higher-energy resolution of the photopeak in the γ spectrum compared to the α spectrum. Presented in Fig. 3.19 is a part of the α-γ coincidence matrix, where diagonal bands of such transitions are visible each of which represents the decay into a given state of the nucleus. The different decay channels can be separated by applying narrow cuts on this matrix. Within a given uncertainty, the condition of equal excitation and decay energies can effectively separate low-spin states of interest. Transitions subject to this condition decay predominantly to the ground state and is represented in the uppermost diagonal band in the matrix. The preceding band depicts decays into the first excited state in ^{24}Mg, namely the E(2^+) = 1368-keV state. Therefore the difference in excitation and decay energies for transitions from this band is exactly the width of the state, 1368 keV. Other noticeable features in the coincidence matrix includes the almost continuous horizontal line at decay energy 1368 keV, stemming from the 2^+ state after being populated by higher-lying excitations as well as the short horizontal bands situated higher up at excitation energies above the particle threshold [5].

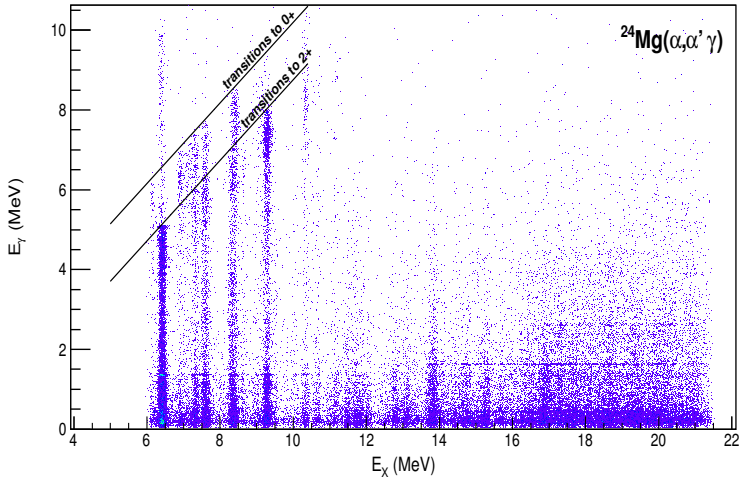

Figure 3.19: *The α-γ coincidence matrix shows the γ-decay energy, E_γ, versus the excitation energy, E_X, for the experiment on ^{24}Mg for one Clover. The diagonal bands marks out the regions of ground state decays and decays into the 2^+ state.*

Thus the knowledge of the excitation and decay energies allows us to make strategic selections on the data, permitting an analysis of each transition individually and allowing one to extract cross sectional information of interest.

3.5 Cross Sections

The ability to make informed data selections on the α-γ coincidence matrix grants us direct access to the cross-sectional data. Low-lying excitations below the particle threshold decay predominantly to the ground state, in comparison to states with higher spins. Therefore, the condition of equal excitation and decay energy, $\mid E_x - E_\gamma \mid \leq 100$ keV, applied to the coincidence matrix is an effective way to separate these E1 low-spin states of interest. Decays to the first excited state can be selected in the same manner, namely by applying the additional condition, $\mid E_x - E_\gamma - E_2^+ \mid \leq 100$ keV to the coincidence matrix. In Fig. 3.20 (a) and (b) a comparison is made for the summed γ spectra either with the coincidence condition only or additionally with the condition $\mid E_x - E_\gamma - E_2^+ \mid \leq 100$ keV, selecting decays to the first excited state. The spectrum in Fig. 3.20 (b) is virtually background free displaying all the decays to the first excited state of ^{24}Mg.

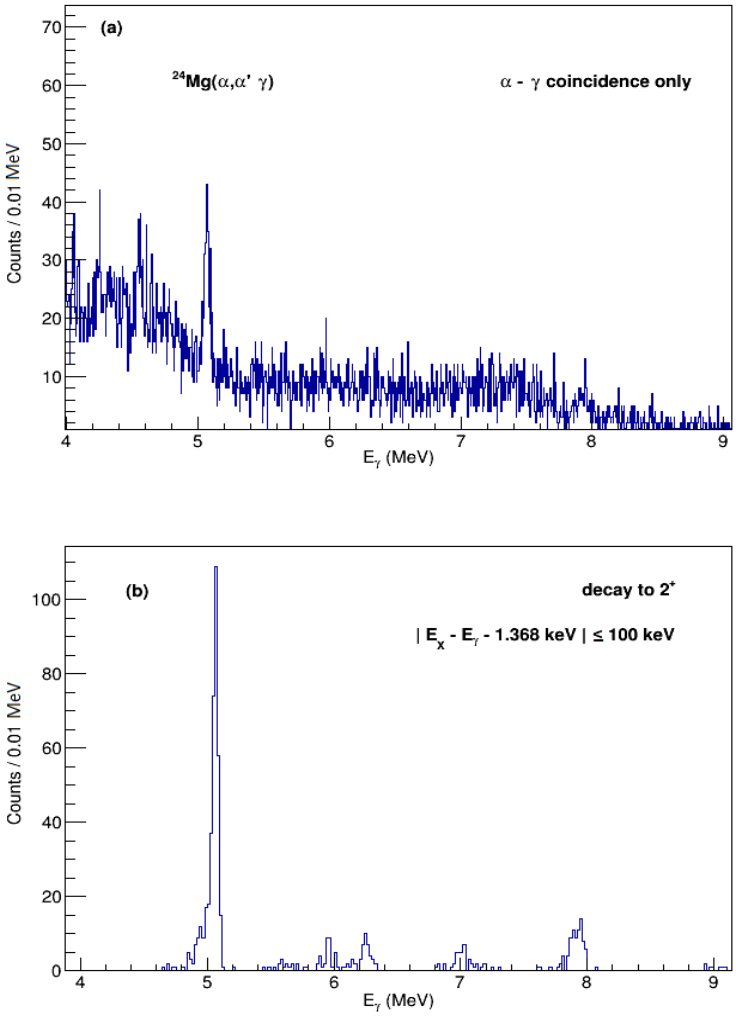

Figure 3.20: *A comparison of the summed γ spectra, where in (a) the α-γ coincidence condition is applied only and in (b) the additional condition $\mid E_x - E_\gamma - E_2^+ \mid \leq$ 100 keV (decays to the first excited state) is applied.*

For the purpose of obtaining the cross sections, as long as the decay can be separated in the γ-spectrum projection this approach enables us to determine the double-differential cross sections of excitations for each individual state. The relation to the single-differential cross section is given by

$$\frac{\mathrm{d}^2\sigma}{\mathrm{d}\Omega_\alpha \mathrm{d}\Omega_\gamma} = \frac{1}{4\pi}.\frac{\Gamma_0}{\Gamma}.W(\mathrm{d}\Omega_\gamma).\frac{\mathrm{d}\sigma}{\mathrm{d}\Omega_\alpha} \quad , \tag{3.5.1}$$

where $\frac{\Gamma_0}{\Gamma}$ is the branching ratio of the γ decay to the ground state and $W(\mathrm{d}\Omega_\gamma)$ is the α-γ angular correlation [38]. As mentioned, this (α, α' γ) experimental technique uniquely allows us to determine the decay patterns of excitations. As described above, by selecting the decays to excited levels via software gates on the excitation spectra (refer to Fig 3.20 (a), (b)), background in the γ spectrum can again be suppressed making it possible to observe almost all branchings to the selected state. This way various branching ratios for a particular state can be obtained.

Given equation 3.5.2 the following connection can be made between the peak area A_i in one of the Clover detectors and the double-differential cross section,

$$A_i = N_t \cdot N_\alpha \cdot \Delta\Omega_\alpha \cdot \Delta\Omega_{\gamma,i} \cdot \epsilon_{int,i}(E_\gamma) \cdot \Delta_{live,i} \cdot \frac{\mathrm{d}^2\sigma}{\mathrm{d}\Omega_\alpha \mathrm{d}\Omega_\gamma} \quad , \quad (3.5.2)$$

where N_t is taken as the number of target nuclei per unit area, N_α is the number of incident α particles, $\Delta\Omega_\alpha$ the opening angle of the spectrometer, $\Delta\Omega_{\gamma,i}$ the opening angle of the ith Clover detector, $\epsilon_{int,i}(\mathrm{E}_\gamma)$ the intrinsic efficiency of the ith Clover detector, and $\Delta_{live,i}$ the live time of the ith Clover detector which is defined as the ratio between the the live and measuring times [38]. For a more detailed description of the above method for determining the double-differential and the accompanying procedures, refer to references [4, 11, 12].

With relation to the α-γ angular correlation, for transitions of different multipolarities different relative intensities should be observed depending on the angle of the HPGe Clover detector. The data points of the angular correlation depend on the scattering angles of the α particles in relation to the γ rays, which in turn are dependent on the recoil angel of the scattered target nucleus. Through inspection of these relative intensities as a function of Clover detector angel we witnessed no angular correlation of the decay transitions. This observation will be addressed and discussed later.

Chapter 4

Results and Discussion

For the purpose of establishing the feasibility of this study, the main results of the experimental coincidence measurements and the accompanying features observed will be thoroughly discussed in this chapter. This includes techniques used to optimize and extract meaningful results as well as interesting effects not entirely predicted. A prominent feature of this coincidence measurement technique is its excellent selectivity and resolving power of transitions from excited states on an event-by-event basis. This will be illustrated as a means to a source of nuclear structure information, with the functionality of the decay detection systems being one of the main aspects of interest.

4.1 Detection Efficiency

4.1.1 Absolute and Intrinsic Efficiency

To gain a better overall understanding of detector efficiency is often convenient to divide efficiencies up into two main classes, namely, absolute and intrinsic.

A prominent feature of the absolute efficiency is its dependence on the exact geometrical spacing of the detection array, the properties of the detector, as well as on γ-ray energy. These dependencies include variables such as the distance from the source to the detector as well as the dimensions and make-up of the detector volume. Consequently, the absolute efficiency is primarily concerned with the coverage of the detection volume seen by an isotropic source. The fraction of the total 4π solid angle subtended by the detection volume plays an important role and is taken into account. The absolute efficiency is defined as

$$\epsilon_{abs} = \frac{\text{Number of events registered}}{\text{Number of photons emitted by the source}} \quad . \tag{4.1.1}$$

On the contrary, the intrinsic efficiency portrays a much lesser geometric dependence, as it is rather more centralized around the likelihood of an incident photon being detected in the detection volume. The quantity too depends on the detector material as well as on the energy of the radiation but to a much lesser extent as well. It is defined as ratio of recorded events to the total number of photons incident on the detector volume,

$$\epsilon_{int} = \frac{\text{Number of events registered}}{\text{Number of photons incident on the detector}} \quad . \tag{4.1.2}$$

Furthermore, for an isotropic source the two efficiency classes are related by

$$\epsilon_{int} = \epsilon_{abs} \times \frac{4\pi}{\Omega} \quad , \tag{4.1.3}$$

where Ω is the solid angle subtended by the detector in relation to the source.

From an experimental view point, the peak efficiency (PE), most commonly referred to as the Full Energy Peak Efficiency (FEPE), is the preferred quantity owing to the fact that the number of events depositing full energy is unambiguous and is not affected by scattering from surrounding objects. It assumes that only the interactions that contribute to the photopeak be counted, i.e. those that deposit full energy of the impinging radiation. Thus the number of events in this case is the integral of the area under the photopeak. Peak efficiencies, specifically for Germanium detectors can be presented in several different ways. The quantity often used and which is directly measurable is the absolute FEPE, defined here as the number of counts in the photopeak divided by the number of γ rays emitted by the source (refer to equation 4.1.4). For the scope of our investigation due to the coincidence setup, the equivalence of this quantity would be the ratio of counts in the photopeak of a particular transition to the number of counts populated in the corresponding state.

$$\epsilon_{\text{abs peak}} = \frac{\text{Number of photopeak events}}{\text{Number of photons incident on the detector}} \tag{4.1.4}$$

4.1.2 HAGAR Efficiency

As a degree of comparison the poor resolution large NaI crystal from HAGAR as well as the superior HPGe Clover detector in this regard were used as ancillary detectors. Although, having a much lower resolving power, the HAGAR with its large detecting volume has a relatively high intrinsic efficiency for detecting γ rays of over a few MeV. With typical energies of a few MeV γ rays deposit their energy predominantly through means of Compton scattering and pair production into the volume with the light per interaction visible to each of the 6 active PM-tubes. Here it is a matter of the more PM-tubes there are the more light is detected, greatly improving the signal output. However, due to the solid angle subtended by each PM-tube with regards to the location of a γ-ray interaction, each PM-tube sees a different amount of light. This degrades the resolution of the detector by at least a factor of two.

In order to calibrate for efficiency, this effect has to be corrected for. By adding up the signal contributions of each PM-tube and averaging over them this improved signal output is achieved, enhancing the resolution in the photopeak. Fig. 4.1 demonstrates this with a projection onto γ-decay energy gated for well defined state in the excitation and summed over all 6 active PM-tubes using the averaging technique described. Comparing this to Fig. 3.11 in section 3.3.1 for the projection of a single PM-tube, the resolution increase is apparent.

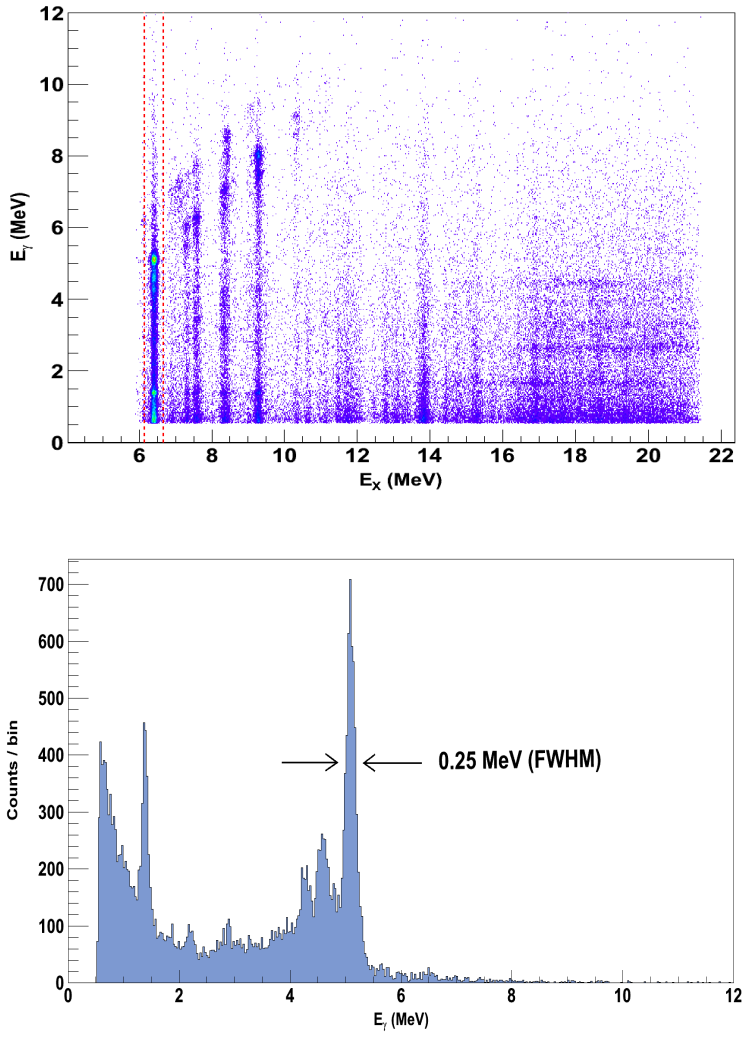

Figure 4.1: *The top figure illustrates the excited state selection within the excitation spectrum from the 2-D coincidence matrix from HAGAR. For the projection onto decay energy in the bottom figure the resolution for a particular transition is given and compared to Fig. 3.11 before averaging, the resolution increased by a factor of more than 2.*

Using in-beam data we constructed a plot of efficiency points for the HAGAR as a function of decay energy. Based on the definition of the absolute FEPE described in the previous section, efficiency data entails determining the exclusive γ-ray yield per transition in relation to the inclusive yield of the corresponding excited state. Corrected for the branching ratios of each decay transition an efficiency point as a function of E_γ is calculated as

$$\epsilon_{\text{abs peak}}(E_\gamma) = \frac{\gamma - \text{ray yield per photopeak}}{\text{Inclusive excited state yield} \times BR} \quad , \tag{4.1.5}$$

where BR is the branching ratio. This procedure is followed for all the prominent decay transitions visible in the decay spectrum. Fig. 4.2 represents such an efficiency plot of the HAGAR for the decay information displayed in Table 4.1. Note the 2193-keV γ efficiency point is not displayed in Fig. 4.2 due to its low counts within the decay spectrum for HAGAR.

Experimental ^{24}Mg Energy Level, E_{level} [MeV]	J^π	Decay energy, E_γ [Mev]
6.432	0^+	1.368
		2.193
		5.063
7.616	3^-	6.246
8.357	3^-	6.988
9.305	0^+	7.935

Table 4.1: *Decay energy information for absolute FEPE calculations. The γ's from the 6432-keV state in ^{24}Mg is a result of decay chains and do not necessarily originate from the that particular excited state.*

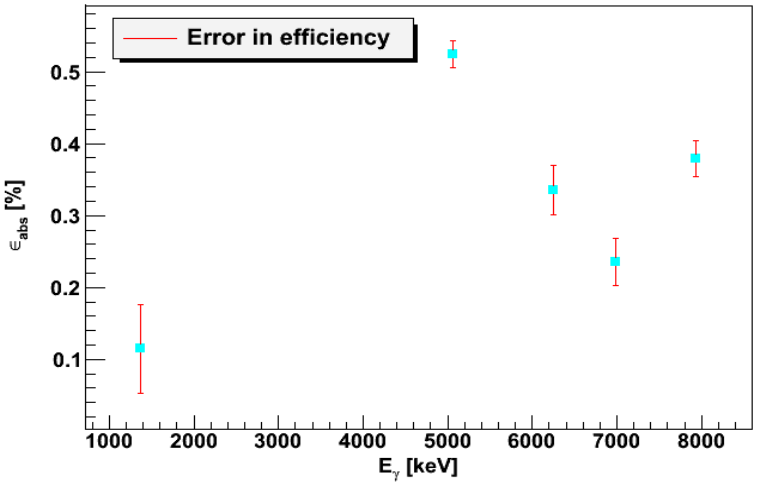

Figure 4.2: *Absolute FEPE curve for the HAGAR as a function of decay energy.*

The 1368 keV energy level is the 2^+ first excited state and is readily populated by higher lying states. A careful treatment of the efficiency for the 1368 keV

γ-ray transition is thus necessary. To verify the calculation of each 1368 keV γ-ray efficiency point, the point itself as well as its error is plotted against the weighted mean and its corresponding standard deviation spread in Fig. 4.3. Thus the 1368 keV γ-ray efficiency point in Fig. 4.2 represents the weighted mean efficiency and the error for a weighted mean. The details regarding the error analysis will be discussed in the subsection to follow (see section 4.1.2.1).

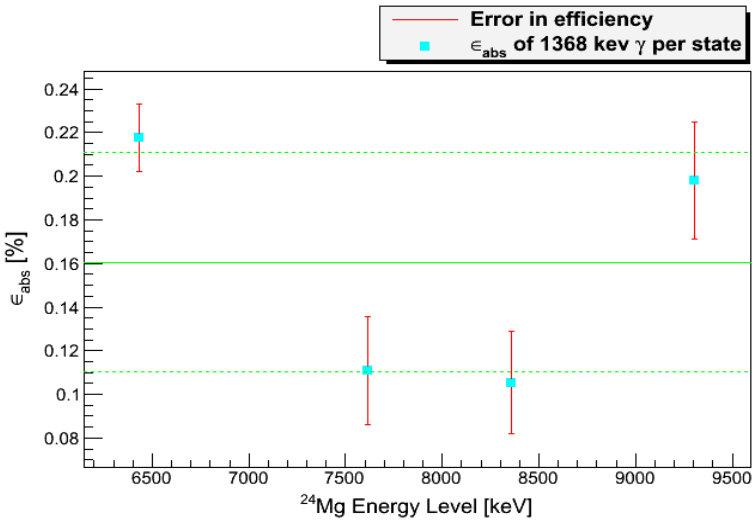

Figure 4.3: *Absolute FEPE of the 1368 keV γ-ray per state plotted against its weighted mean.*

Using expression 4.1.3, where the intrinsic efficiency is given in terms of the absolute efficiency, the intrinsic efficiencies can be computed provided that the solid angle for HAGAR is calculated. The proportionality constant between the two efficiency classes is what is known as the geometrical efficiency, $\frac{\Omega}{4\pi}$, and in this case it is the fraction of the solid angle subtended by the HAGAR in relation to a 4π sphere. Thus to obtain ϵ_{int} the number of counts in the excited state is firstly scaled by the geometrical efficiency constant and the efficiency is then recalculated. Fig 4.4 is a plot of the intrinsic efficiency curve for the HAGAR.

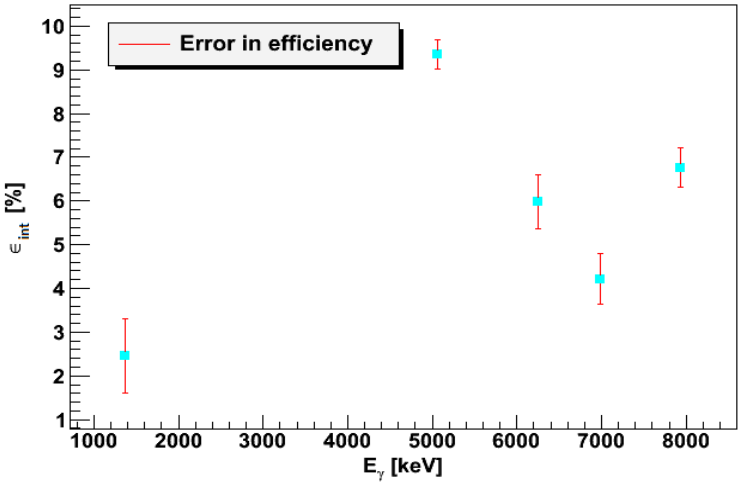

Figure 4.4: *Intrinsic efficiency curve for the HAGAR as a function of decay energy.*

To comment on the efficiency plots for the HAGAR, as expected for sufficiently high γ-ray energies the efficiency exponentially falls off with increasing E_γ. However, we expect this trend to extend from energies greater than a few keV all the way to the MeV range, instead we observe a relatively low efficiency for the 1368 keV γ ray. The accuracy of this observation is verified in Fig. 4.3 given that all the 1368 keV efficiency points per state fall within the standard deviation of the weighted mean. A possible explanation could be that based on the make up of the detector i.e. dead layer, detector casing material etc..., γ rays below a certain threshold energy (1368 keV γ ray included) are attenuated more than for γ rays above this threshold. This why we see a peak in efficiency for the 5063 keV γ ray. Furthermore, the main reason for a dip in efficiency at decay energy of 6988 keV is the low photopeak yield relative to the state yield.

4.1.2.1 Error Analysis

An initial error analysis treatment for the HAGAR entailed the validation of the efficiency for detecting the 1368 keV γ-ray. From Fig. 4.3 the weighted mean is calculated using the standard formula for weighted data points, namely,

$$\bar{x} = \frac{\Sigma_{i=1}^{n} w_i x_i}{\Sigma_{i=1}^{n} w_i} \quad , \tag{4.1.6}$$

where the branching ratios for the different transitions are used as weights w_i and x_i represent the efficiency data points. The variance of a weighted mean, $\bar{x}$, differs from that of an unweighted mean and is given by the expression,

$$\sigma^2_{weighted} = \frac{\Sigma^n_{i=1} w_i (x_i - \mu^*_i)^2}{\Sigma^n_{i=1} w_i} \quad , \tag{4.1.7}$$

where $\sigma_{weighted}$ is the standard deviation for the weighted mean and is displayed by the dashed lines in Fig. 4.3.

Governed by expression 4.1.5, the error involved in calculating the absolute peak efficiency, namely $\sigma_{\epsilon_{abs}}$, includes the error in the exclusive photopeak γ yield, σ_{excl}, as well as the error in the inclusive excited state yield, σ_{incl}. Thus the error in these two quantities are to be combined in quadrature as follows,

$$\left(\frac{\sigma_{\epsilon_{abs}}}{\epsilon_{abs}}\right)^2 = \left(\frac{\sigma_{excl}}{\text{exclusive counts}}\right)^2 + \left(\frac{\sigma_{incl}}{\text{inclusive counts}}\right)^2 \quad , \tag{4.1.8}$$

where ϵ_{abs} is the absolute peak efficiency and the exclusive and inclusive counts refer to the yield in the photo peak and the excited state corrected for the branching ratios respectively. Consequently, there is a secondary error inherent within each of the errors in the above expression. The yield from the corresponding peaks within the gamma and focal plane spectra are extracted from the peak areas. Thus the errors in both σ_{excl} and σ_{incl} further includes an error in fitting the data as well as the statistical error in the number of counts extracted.

With regards to the intrinsic efficiency data, the error is computed by simply scaling the error in the absolute peak efficiency, $\sigma_{\epsilon_{abs}}$, by the geometrical efficiency constant, i.e. $\frac{\Omega}{4\pi}$. The error in the solid angle is not considered as it is negligible in comparison the the fitting and statistical errors.

4.1.3 Clover Efficiency

Following a similar procedure as in section 4.1.2 the efficiency of the Clover detectors are presented here. The only difference in approach being the manner in which the contributions of each Clover diode is summed up as well as the extraction of yield in the decay energy spectra for the various photopeaks. Due to the nature of the Clover‘s electronics, a summing technique referred to as addback was implemented. The result is decay spectra with substantial photopeak yield aiding the process of peak-efficiency data calculations.

A limitation feature of the Clover detectors are its relatively low efficiencies. Using the in-beam data to calculate efficiencies, the high energy γ’s suffer

from statistics making the extraction of photopeak counts increasingly difficult. Where possible the conventional fitting method was used to obtain the true photopeak yield, besides where the yield becomes considerably low and these methods fail. In these cases the best approach to accurately estimate yield is by integrating over the photopeak region in the spectrum. At this stage due to low statistics background is not a major contributing factor allowing this integration method to extract photopeak counts that are fairly close to the true yield. This adaptation has a direct effect on the error analysis which will be discussed in the subsection to follow.

For the Clover detectors to further reveal the trend of the efficiency points both the in-beam and ^{60}Co calibration run data were used. Fig. 4.5 and Fig. 4.6 represents the absolute FEPE, firstly of the 1368 keV γ ray per state and secondly as a function of E_γ for the two Clover detectors. In both cases for the upper plot the weighted mean of the 1368 keV γ ray is plotted with its corresponding error.

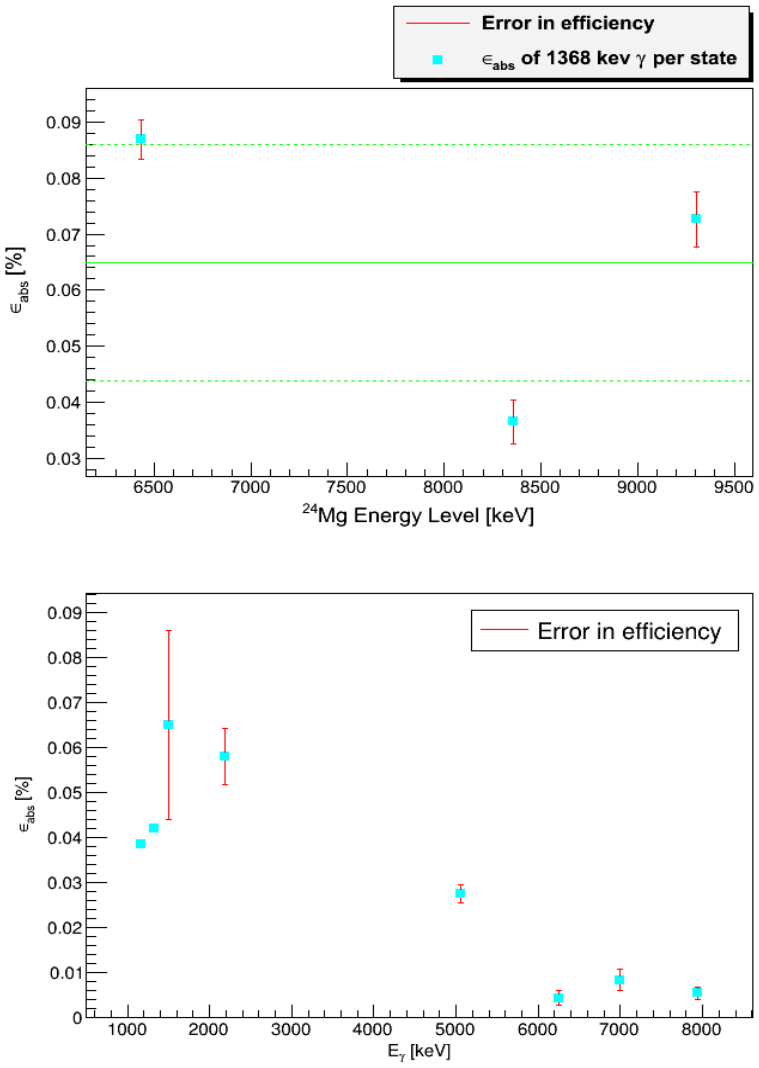

Figure 4.5: *Absolute FEPE of the 1368 keV γ ray per state plotted against its weighted mean. The bottom figure illustrates the absolute efficiency for the 90° Clover detector as a function of decay energy.*

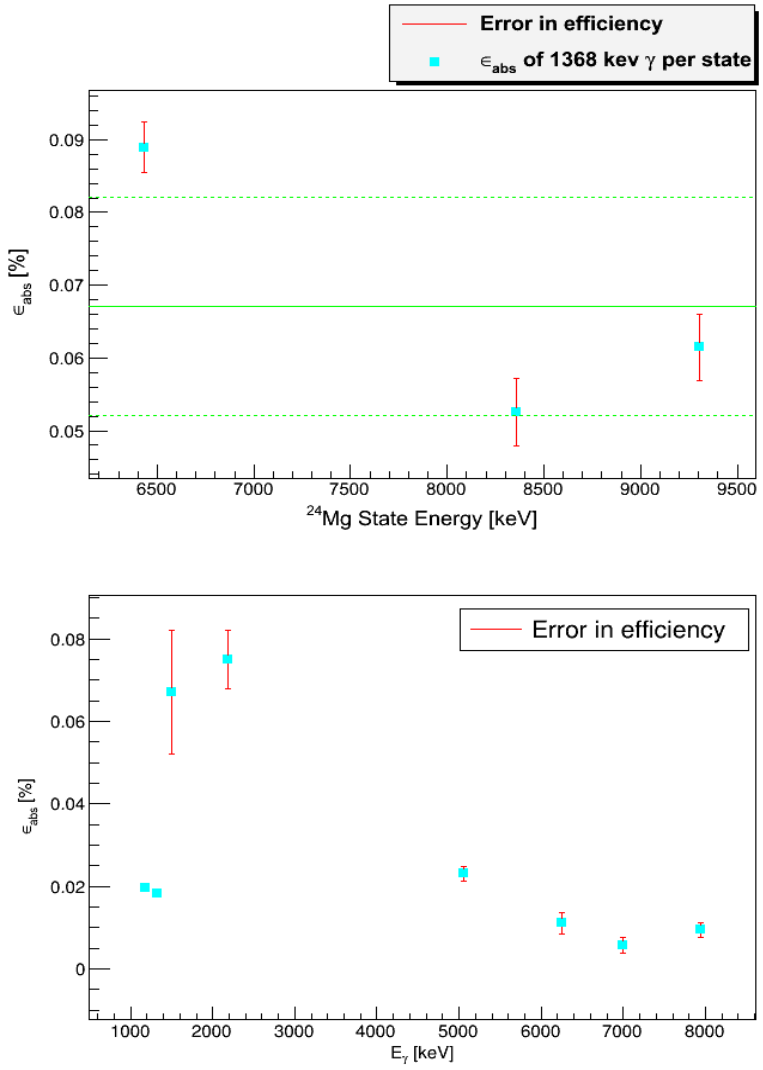

Figure 4.6: *Absolute FEPE of the 1368 keV γ-ray per state plotted against its weighted mean. The bottom figure illustrates the absolute FEPE for the 147° Clover detector as a function of decay energy.*

By means of a solid angle calculation for the two Clover detectors, the geometrical and in turn the intrinsic efficiency can be determined by the same method followed for the HAGAR using the absolute FEPE (refer to equation 4.1.3). Fig. 4.7 is a plot of the intrinsic efficiencies for the dominant decay transitions detected in the 90° and 147° Clovers respectively.

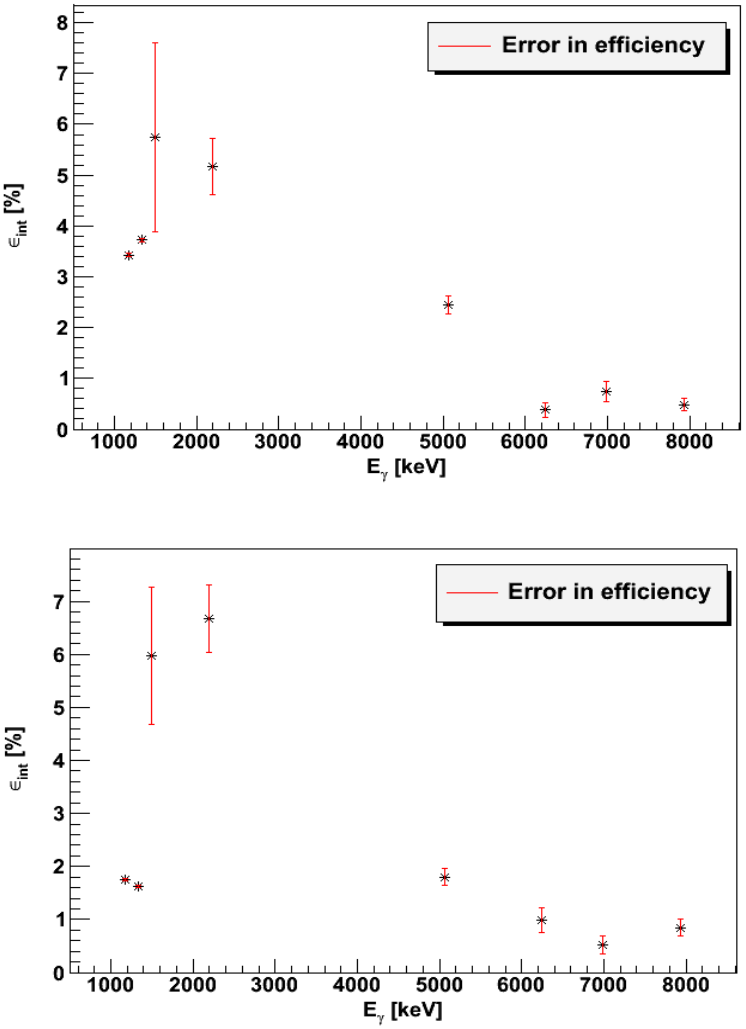

Figure 4.7: *Intrinsic efficiency for the 90° and 147° Clover detectors, incorporating the fraction of the solid angle subtended by the Clover.*

For both Clover detectors the two initial calibration run ^{60}Co efficiency points(i.e. γ energies 1173 and 1332 keV) in the absolute and intrinsic cases come at considerably lower efficiency than the 1368 keV efficiency point. As a consequence of their low errors, which can be attributed to their high photopeak yield, the ^{60}Co efficiency points for both the absolute and intrinsic cases are disregarded. With reference to the trend of the efficiency plots for both Clovers we witness the exponential decrease in efficiency for increasing decay energy within the experimental errors. For the high energy efficiencies besides their low yield, it was possible to extract efficiencies with reasonable errors. A promising feature

is the similarity in the trends of the higher energy efficiencies between the HAGAR and Clover efficiency plots.

4.1.3.1 Error Analysis

A treatment of the Clover efficiency errors entails the same procedures followed for the HAGAR, except for the error involving the extraction of the photopeak counts in the decay spectra. Due to the integration method used, only the statistical error present in the number of counts contributes towards the overall exclusive error. With regards to the inclusive yield, the error analysis is unchanged where by the fitting method is used to estimate the photopeak yield. Furthermore, the intrinsic efficiency errors are scaled in the same manner by the geometrical efficiency as in the case of the HAGAR detector.

4.1.4 Gamma Coincidence Rate

The choice of both high and low resolution γ detectors were available in the form of the Clover and the large NaI Hagar detectors. The functionality of the Clover detectors was a priority since emphasis was put on the high resolution capabilities achievable though the setup. With regards to its efficiency, an important conclusion would be the rate of coincidence detection for the Clover detectors during an experiment in which subsequent γ decay is present. This would benefit the planning of future projects as a means to enhance statistics which is an apparent limitation to the current coincidence setup consisting of only the two Ancillary Clover detectors. As a method of estimation the γ count rate per shift per clover can be calculated by

$$R \quad = \quad \epsilon \cdot N \cdot I \cdot \frac{d\theta}{d\Omega} \cdot \Delta\Omega \quad , \tag{5.1}$$

where

- ϵ is the single Clover efficiency,
- N is the number of target ions (in ions/cm^2),
- I is the particles per second of beam (in pnA),
- $\frac{d\theta}{d\Omega}$ is the differential cross section (in mb/sr), and
- $\Delta\Omega$ is the solid angle of the K600 (in sr).

For two distinct cases, namely at the low energy and high energy regions of the efficiency plots, for Clovers 1 the count rates per shift (typically 8 hour long shifts) are calculated. Firstly, equation 5.1 is rewritten with the constants condensed into one,

$$R \quad = \quad C \cdot N \cdot I \cdot \frac{d\theta}{d\Omega} \quad , \tag{5.2}$$

with C being the proportionality constant. Thus for,

Case 1: A 1.368 MeV γ ray with;

- $\varepsilon_{abs} = 0.0649$ %,
- a fixed K600 aperture of $\Delta\Omega = 4.39$ msr,
- a differential cross section $\frac{d\theta}{d\Omega} = 0.1$ mb/sr,
- $I = 1$ pnA, and
- $N = 5.24 \times 10^{19}$ ions/cm2 for a 2.1 mg/cm^2 thick target,

the count rate per shift for Clover 1 is R = 2.69.

Case 2: A 6.246 MeV γ ray with;

- $\varepsilon_{abs} = 0.004295$ %,
- a fixed K600 aperture of $\Delta\Omega = 4.39$ msr,
- a differential cross section $\frac{d\theta}{d\Omega} = 0.1$ mb/sr,
- $I = 1$ pnA, and
- $N = 5.24 \times 10^{19}$ ions/cm2 for a 2.1 mg/cm^2 thick target,

the count rate per shift for Clover 1 is R = 0.178 particles.

It is important to note 1 pnA translates to a beam of 6.25×10^9 particle/sec with $\Delta\Omega$ being a constant of the K600 setup. For higher γ energy per 8 hour shift the count rate drops by as much as a factor of 15 and this is fairly consistent with our measured data. We observe significant drops in photopeak yield for decay transitions from 5 to 8 MeV.

To further characterize the γ count rate in the Clover detectors, consider differential cross sections typical to (α, α') reactions at zero degrees. In the search for α-condensed states, inelastic α scattering was performed on ^{24}Mg (See ref. [40]). Measured differential cross sections for low lying states in ^{24}Mg range from 10 to 100 mb/sr. A cross section of 100 mb/sr was measured for the 0^+ 6.342 MeV state at zero degrees. The count rates for these upper and lower limit cross sections using the same values as previously were calculated as $R(10\ \text{mb/sr}) = 268.73$ and $R(100\ \text{mb/sr}) = 2687.3$ particles/shift. The differential cross section, largely dependent on θ_{lab}, has a significant effect on the γ yield within the Clover detectors. Ideally, operating at forward angles would increase yield if this is the desired outcome.

Furthermore, the beam intensity and target thickness could be optimized to achieve maximal count rates at the desired high resolution, however in both cases the risk of degrading the resolution is evident. For increased target thickness the collision probability rises, however, with the undesired effect of an increased particle flux and in turn background in the focal plane. A positive change in the beam intensity has the same effect.

4.2 α - γ Angular Correlation

As a means to test its feasibility, for the first time at iThemba LABS an (α, $\alpha'\gamma$) coincidence measurement at $\theta = 0^\circ$ was performed using the K600 magnetic spectrometer to magnetically analyse reaction products. This experimental method proved to be highly selective to low natural parity transitions, with the combination of γ spectroscopy allowing a detailed analysis of the decay on a state-by-state basis. Due to this fact it was expected that a clear α - γ angular correlation would be witnessed. However, this was not the case given that for both Clover detectors no distinction could be made with regards to the relative intensities of each decay transition. A kinematics calculation of the scattering process revealed that at zero degrees there is a large spread in the recoil scattering angle. In essence this means that there is no preferred dominant direction for emitted γ rays as their direction of propagation is dependent on the recoil scattering angle. Thus as a direct consequence of the kinematics, if any angular correlation exists it would be wiped out.

4.3 Beyond Particle Threshold

Going to excitation energies above the particle threshold ($S_p = 11.69$ MeV, $S_n = 16.53$ MeV, $S_\alpha = 9.31$ MeV) we observe γ-rays corresponding to the decays of excited states in a number of compound nuclei formed. This way the energy dependence of the decay of excitations above the particle threshold

can be studied. More specifically the energy-dependent branchings of particle decays of ^{24}Mg to various levels in the daughter nuclei as well as information about particle decay patterns of excitations above the threshold is obtainable. Fig. 4.8, portrays the γ-spectra projections for different regions within the excitation spectrum.

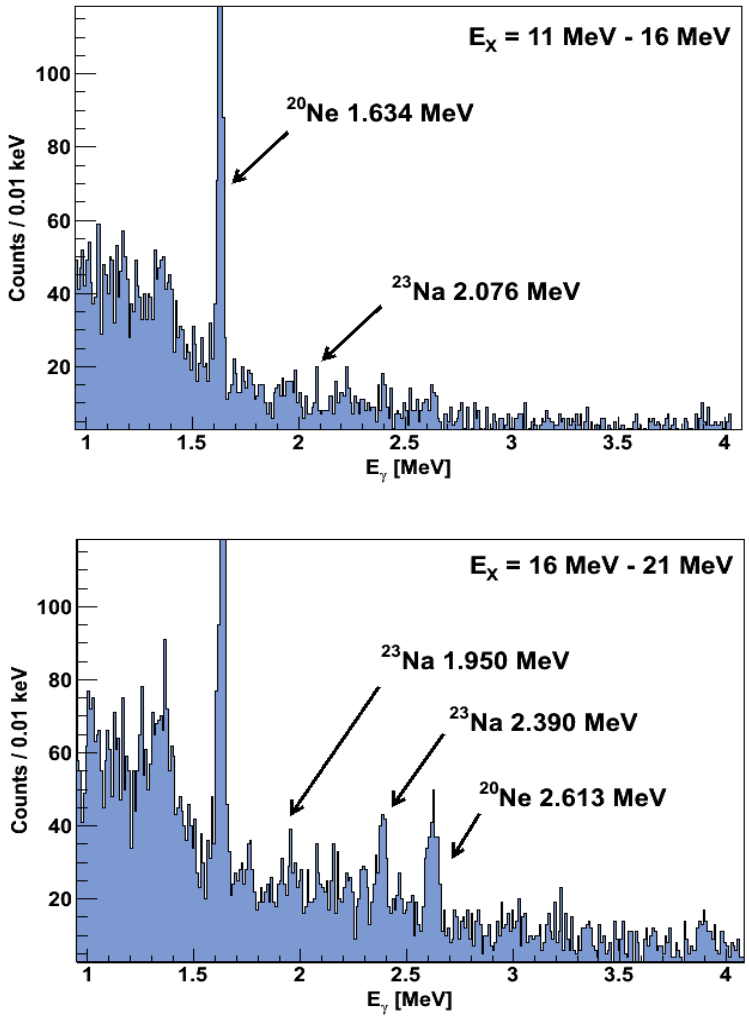

Figure 4.8: *Decay transitions beyond the particle threshold for excitation energy regions E_x = 11 MeV - 16 MeV and E_x = 16 MeV - 21 MeV. The decays corresponding to the compound nuclei ^{20}Ne and ^{23}Na.*

Namely, the excitation energy regions E_X = 11 MeV - 16 MeV and E_X = 16 MeV - 21 MeV are projected onto γ energy with decays from excited states in

^{20}Ne (corresponding to α-particle emission) and ^{23}Na (corresponding to proton emission) are clearly visible.

4.4 BACTAR

An important feature to mention involving the measurements on two other targets with higher Z-values than ^{24}Mg, namely ^{58}Ni (2.1 mg.cm^{-2} thick) and ^{208}Pb (2.1 mg.cm^{-2} thick), were the increased decay energy spectrum backgrounds. It has been established that target thickness is directly proportional to increased background in the focal plane. However, targets with increasing Z-value is believed to contribute in this regard as well. The assumption is that as Z increases with more dense targets, more scattered alpha's are produced which in turn interacts with material downstream of the beam. This process occurs through a range of reactions producing an increased flux of particles, of which includes high-energy γ rays. Ideally, this phenomena can be verified by gating on a well defined state within the target nuclei and projecting onto decay energy. Energies greater than the highest transition for the particular state are not permittable and is regarded as background for the high Z-valued nucleus. However, due to the dynamics of the measurement the decay energy spectra are bounded from above thus making a projection on particular transitions in the decay spectra challenging. An alternative means of roughly validating this effect is by superimposing the two decay energy spectra for ^{58}Ni and ^{208}Pb, both normalized to the same beam rate. An increased γ energy background should be witnessed for the higher Z-valued nucleus. To ensure that the beam rate for both decay spectra are the same, the number of incident alpha's is calculated by

$$N_0 = \frac{CII.R.10^{-12}}{e} \quad , \tag{4.4.1}$$

where

- CII is the current integrator scalar read out,
- R is the selected current integrator range (in nA), representing 1000 counts per second for a full scale read-out, and
- e is the electric charge of an α particle.

It is evident that for the same beam rate there is a vast increase in gamma energy background from ^{58}Ni to ^{208}Pb as illustrated in Fig. 4.9. This can be related to the high energy γ's produced from secondary scattering.

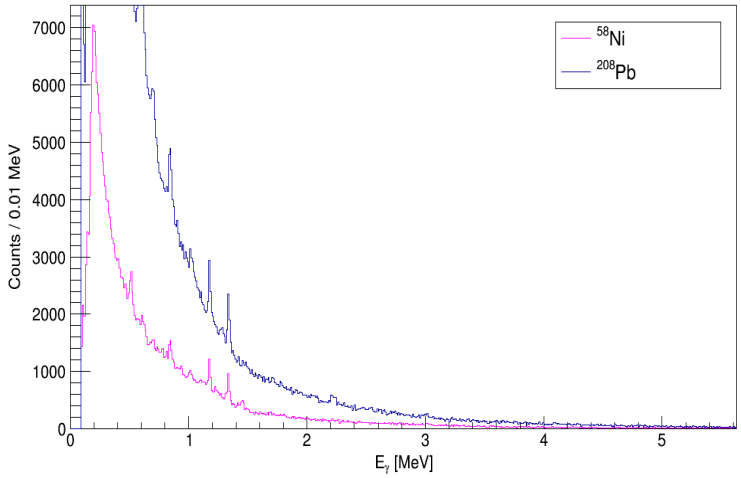

Figure 4.9: *A projection onto decay energy gated for a cutout region in the excitation spectrum. The two decay spectra for ^{58}Ni (pink) and ^{208}Pb (blue) are superimposed, illustrating the increased background for targets with increasing Z value.*

This undesired effect brought about the motivation for a new target chamber development, called BACTAR. The chamber is completely made of aluminium minimizing activation during run time as compared to the previous steel chamber. The main advantage lies in its redesign permitting the chamber to operate at forward angles while greatly reducing secondary scattering of reaction products off exit flanges further downstream. Furthermore, its functionality is enhanced with the capacity to perform scattering experiments with silicon detectors for future projects. Fig. 4.10 is a 3-D representation of the BACTAR scattering chamber.

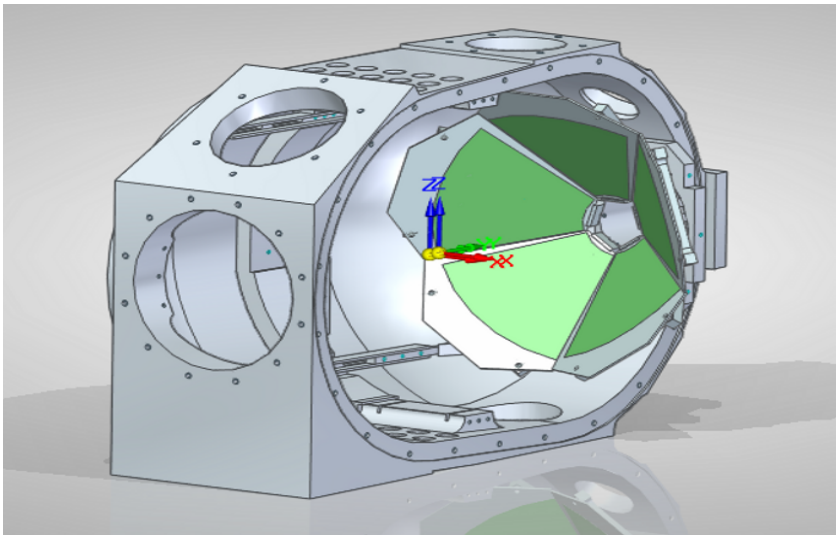

Figure 4.10: *The BACTAR scattering chamber.*

Chapter 5

Summary and Conclusion

As a means to test its feasibility, for the first time at iThemba LABS an (α, $\alpha'\gamma$) coincidence measurement at $\theta = 0°$ was performed using the K600 magnetic spectrometer to magnetically analyse reaction products. This experimental method proved to be highly selective to low natural parity E1 transitions, with the combination of γ spectroscopy allowing a detailed analysis of the decay on a state-by-state basis.

Firstly, as a result of this selectiveness it was expected that a clear α - γ angular correlation would be witnessed. However, by means of a kinematic calculation of the reaction we proved that all angular correlation information is to a great extent wiped out due to the large spread in recoil scattering angle. Specifically, for the Clover detectors this is the case due to the fact that there is no distinction in the relative intensities of each decay transition within the two Clovers.

For the gamma spectroscopy we had a choice of both high resolution and high efficiency γ-ray detectors. As an initial investigation the functionality of the Clover detectors was a priority since emphasis was put on the high resolution capabilities achievable though the setup. Thus an important conclusion would be the rate of coincidence detection for these high resolution Clover detectors. Analysis clearly suggests that low statistics is a definite limitation of the experimental techniques ability to extract meaningful spectroscopic information. Furthermore, these limitations are addressed with ways of minimizing its effects. In this regard maximizing γ yield in the coincident measurement was our key objective. With respect to the γ ray efficiencies for both the Clover and the HAGAR detectors, the contrast of high resolution and high efficiency was then investigated. As a general comment we saw that the similarities not only for the efficiencies of the Clover detectors but too between the Clovers and the HAGAR detector gave us to an extent confidence in our measured results. We also managed to account for inconsistencies in the somewhat unusual ef-

ficiency trends. Overall these results suggest that for low multiplicity events high resolution is not necessarily needed but that knowing how the state decays is sufficient. Thus a prospect could be to instead opt for scintillator type high granularity detectors (e.g. CsI detectors) arranged in a 4π configuration. This would further aid angular correlation calculations by means of correcting for recoil scattering which in our investigation wiped the angular correlation information out due to its large spread.

Thus it can be said based on the findings of this investigation that the study of $(\alpha, \alpha'\gamma)$ coincidence measurement at $\theta = 0°$ is feasible to within the discussed limitations not only of the experimental setup but of the coincident measurement too. Results of similar measurements are to a great extent reproducible with our setup ([5], [11], [38]) and the level of justification for what we observed suggests that we understand our results and more importantly are in a position to correct for certain short comings and improve on this study for future work.

List of References

[1] B. R. Martin, Nuclear and Particles Physics: An Introduction, John Wiley and Sons, Hoboken, USA, (2006).

[2] U. Garg et al., Phys. Rev. Lett. **45**, 1670, (1980).

[3] B. F. Davis et al., Phys. Rev. Lett. **79**, 609, (1997).

[4] T.D. Poelhekken, S.K.B. Hesmondhalgh, H.J. Hofmann, A. van der Woude, M.N. Harakeh, Phys. Lett. B **278**, 423, (1992).

[5] D. Savran et al., Nucl. Instr. and Meth. A **564**, 267, (2006).

[6] N. Ryezayeva *et al.*, Phys. Rev. Lett. **89**, 272502, (2002).

[7] P. Adrich *et al.*, Phys. Rev. Lett. **95**, 132501, (2005).

[8] N. Paar, D. Vretenar, E. Khan, G. Colo, Rep. Prog. Phys. **70**, 691, (2007).

[9] J. J. van Zyl, Masters thesis, Stellenbosch University, unpublished, (2008).

[10] W. E. Burcham, Nuclear Physics: An Introduction, 2nd Edtion, Longman, London, (1973).

[11] D. Savran et al., Phys. Rev. Lett. **97**, 172502, (2006).

[12] J. Endres et al., Phys. Rev. Lett. **105**, 212503, (2010).

[13] W. E. Burcham, Elements of Nuclear Physics, Longman, London, (1979).

[14] R. Neveling, H. Fujita, F.D. Smit, T. Adachi, G.P.A. Berg, E.Z. Buthelezi, J. Carter, J.L. Conradie, M. Couder, R.W. Fearick, S.V. F Ì rtsch, D.T. Fourie, Y. Fujita, J. G Ì rres, K. Hatanaka, M. Jingo, A.M. Krumbholz, C.O. Koreba, J.P. Mira, High Energy-resolution Zero-degree Facility for Light Ion Scattering and Reactions, Nuclear Instruments and Methods in Physics Research A **654**, 29-39, (2011).

[15] The iThemba LABS website, http://www.tlabs.ac.za/public/default.htm, (2009).

[16] R. T. Newman, Ph.D. thesis, University of Cape Town, unpublished, (1996).

[17] R. Neveling et al., Progress report: PR194, iThemba LABS, unpublished, (2013).

[18] M. Freer et al., PRC **80**, 041303(R), (2009).

[19] H. Fujita et al., Nucl. Instrum. Methods Phys. Res. A **484**, 17, (2002).

[20] J.A. Swartz, A Feasibility Study of the (^{3}He,^{8}He) Reaction with the K600 Magnetic Spectrometer, Master's thesis, Stellenbosch University, (2010).

[21] H. E. Wegner et al., Nuclear and Particle Physics Source Book, edited by S. Parker (McGraw-Hill, New York, 1987).

[22] R. Neveling, Master's thesis, University of Stellenbosch, unpublished, (1998).

[23] J.C. Cornell, J.G. de Villiers, D.T. Fourie, iThemba Laboratory for Accelerator Based Sciences (formerly the National Accelerator Center), NAC-Report **92/4**, p. 1, (1992)

[24] Y. Fujita, K. Hatanaka, G.P.A. Berg, K. Hosono, N. Matsuoka, S. Morinobu, T. Noro, M. Sato, K. Tamura, H. Ueno, Nucl. Instr. and Meth. B **126**, 274, (1997).

[25] A. Tamii, Y. Fujita, H. Matsubara, T. Adachi, J. Carter, M. Dozono, H. Fujita, H. Hashimoto, K. Hatanaka, T. Itahashi, M. Itoh, T. Kawabata, K. Nakanishi, S. Ninomiya, A.B. Perez-Cerdan, L. Popescu, B. Rubio, T. Saito, H. Sakaguchi, Y.SakemiY. Sasamoto, Y. Shimbara, Y. Shimizu, F.D. Smit, Y. Tameshige, M. Yosoi, J. Zenhiro, Nucl. Instr. and Meth.A **605**, 326, (2009).

[26] R. Neveling, F.D. Smit, H. Fujita, and R.T. Newma, Guide to the K600 Magnetic Spectrometer, unpublished, (2009).

[27] G. P. A. Berg, C. C. Foster, E. J. Stephenson, and B. F. Davis, K600 Transmission Mode for 0^o Inelastic Scattering, IUCF Annual Report, **106**, (1994).

[28] W. Bertozzi, M.V. Hynes, C.P. Sargent, C. Creswell, P.C. Dunn, A. Hirsch, M. Leitch, B. Norum, F.N. Rad, and T. Sasanuma, *Focal Plane Instrumentation: A Very High Resolution MWPC System for Inclined Tracks*, Nuclear Instruments and Methods, **141**,457-476, (1977).

[29] K.G. Fissum, W. Bertozzi, J.P. Chen, D. Dale, H.C. Fenker, J. Gao, A. Gavalya, S. Gilad, C.R. Leathers, N. Liyanage, R.O. Michaels, E.A.J.M. Offermann, J. Segal, J.A. Templon, R. Wechsler, B. Wojtsekhowski, and J. Zhao, *Vertical Drift Chambers for the Hall A High-resolution Spectrometer at Jefferson Lab*, Nuclear Instruments and Methods in Physics Research A, **474**, 108-131, (2001).

[30] Saint Gobain Crystals, http://www.detectors.saint-gobain.com, (2009).

[31] HPGe Clover detector, http://www.canberra.com/products/detectors/germanium-detectors.asp, (2014).

[32] MIDAS, Data Acquisition System, Paul Scherrer Institute, Switzerland, http://midas.psi.ch, (2009).

[33] ROOT. Version 5.32/00, http://root.cern.ch, (2011).

[34] G. F. Knoll, Radiation Detection and Measurement, 3rd Edition, John Wiley and Sons, Hoboken, USA, (2000).

[35] A. Breskin *et al.*, Nucl. Instr. Meth. **119**, (1974).

[36] J.A. Swartz, Search for low-spin states above the 5-α break-up threshold in ^{20}Ne, Ph.D. thesis, Stellenbosch University, (2014).

[37] C. Wheldon, Derivation for two-body kinematics, unpublished, (2012).

[38] J. Endres et al., Phys. Rev. C **80**, 034302, (2009).

[39] National Nuclear Data Center, www.nndc.bnl.gov/chart, (2014).

[40] T. Kawabata et al., Journal of Physics: Conference Series **436**, 012009 (2013).